

Master Thesis

**Exploring the existence of prebiotic species:
ALMA observations of amine-containing
organic molecule in star-forming regions.**

Harumi Minamoto

17M01629

Nomura Laboratory

Department of Earth and Planetary Sciences, Tokyo Institute of Technology

January 18, 2019

Abstract

A variety of complex organic molecules have been observed for decades in the interstellar medium. Some of them are considered to be delivered to the primordial Earth by comets, and contributed to the chemical evolution leading to terrestrial life. One example of such prebiotic species is amino acid. Glycine, the simplest amino acid, has been detected in comet 67P/C-G but its presence in molecular clouds is still uncertain.

In this work we analyze the ALMA archival data toward 3 star-forming regions, Orion Kleinmann-Low nebula (hereafter Orion-KL), IRAS 16293-2422 (IRAS 16293), and L483, to search methylamine (CH_3NH_2), which is suggested as precursors to glycine.

As a result of analysis, we found 8 candidate emission at the hot core region in Orion-KL. By using the rotation diagram method, we evaluated its tentative column density and rotational temperature to be $5.5 \times 10^{14} \text{ cm}^{-2}$ and 93.3 K, respectively. On the other hand, CH_3NH_2 is not detected and stringent upper limit column densities are determined in IRAS 16293 and L483.

Contents

Abstract	i
1 Introduction	1
1.1 Glycine and methylamine	1
1.2 Star forming region	2
1.2.1 Orion Kleinmann-Low nebula	2
1.2.2 IRAS 16293-2422	2
1.2.3 L483	2
1.3 Radio observation	2
1.3.1 Atacama Large Millimeter Array	3
1.4 Purpose of this work	3
2 Methylamine survey in Orion-KL	4
2.1 Observation data	4
2.2 Analysis	5
2.2.1 Continuum Subtraction of SV data	5
2.2.2 Line identification	6
2.3 Results	7
2.3.1 Transitions	7
2.3.2 Distribution	8
2.3.3 Spectrum	18
2.4 Disucssion	19

2.4.1	Column density and Rotation temperature	19
2.4.2	Blending	20
3	Methylamine survey in low mass star-forming regions	21
3.1	Review of low mass star-forming region	22
3.2	Analysis	22
3.3	IRAS 16293	22
3.3.1	Observation data	22
3.3.2	Results	22
3.4	L483	24
3.4.1	Observation data	24
3.4.2	Results	24
4	Discussion	26
5	Conclusions	27
A	Distribution of methylamine lines contaminated by other molecular line emission in Orion-KL	28
A.1	Integrated intensity maps	28
A.2	Channel maps	32
Acknowledgments		48
References		49

Chapter 1

Introduction

1.1 Glycine and methylamine

Methylamine is considered as a precursor of the simplest amino acid glycine. Recent experimental studies have shown several reaction pathways to forming glycine in water containing ices starting from CH₃NH₂ and CO₂ subjected to high energy electrons (Holtom et al. 2005) or UV radiation (Bossa et al. 2009; Lee et al. 2009). Under similar conditions glycine can decompose to yield methylamine and CO₂ (Ehrenfreund et al. 2001). Interstellar methylamine was first detected toward Sgr B2 at 3.5 cm (Fourikis et al. 1974) and at 3mm (Kaifu et al. 1974). Recently, methylamine has been detected in a spiral galaxy with a high redshift of 0.89 located in front of the quasar PKS 1830-211 (Muller et al. 2011). It was also observed in cometary samples of the Stardust mission (Glavin et al. 2008).

図(??)にメチルアミンの構造を示す。

1.2 Star forming region

1.2.1 Orion Kleinmann-Low nebula

今回の研究対象としているこの Orion Kleinmann-Low (KL) 天体はオリオン星雲の中にある赤外線星雲であり、太陽からおよそ 437 pc (約 1425 光年) 離れた位置に存在している [21]。この領域では、太陽の 30 倍の質量をもつ巨大な星が誕生している非常に活発な領域であり、広い範囲の周波数を観測する line survey でも数多くの分子が観測されている [5, 22]。この Orion KL は太陽から最も近い位置にある大質量星形成領域であり、放射強度も強く、なおかつ多くの分子が存在するため、この領域に関しては 1967 年に発見されて以来、line survey を含めた多くの研究が今までにもなされている。Orion-KLにおいて、多くの有機分子が存在する領域として Hot core と Compact ridge と呼ばれる場所が知られている。Hot core は暖かく (~ 150 K)、コンパクト (<0.05 pc) で、密度の高い (10^6 cm⁻³) 領域として知られており [23]、Compact ridge も同様に暖かく密度の高い領域であることが分かっている [24]。しかし、化学的な性質は異なっており、Hot core では窒素を含む分子（たとえば、NH₃、CH₃CN など）が多く観測される一方で、Compact ridge では酸素を含む分子（たとえば、CH₃OH、CH₃OCH₃ など）が多く発見されている [24]。

1.2.2 IRAS 16293-2422

1.2.3 L483

1.3 Radio observation

電波による宇宙空間の観測は、Karl G. Jansky による 1930 年代の初めての宇宙電波の発見、Grote Reber による世界初の電波望遠鏡の作成以来、宇宙空間の観測方法の 1 つとして確立し、また、第 2 次世界大戦中のレーダー技術の進展を受けて大きな進展を遂げている。これ以降、X 線や赤外線などの波長でも観測が行われるようになり、可視光だけではわからない数々の宇宙の不思議を解き明かしている。ただし、

大気による吸収の影響で、全波長のうち地上から観測可能なのは可視光と電波、赤外線の一部となっている。電波の領域では、20 MHz 以下の周波数は電離層を通りず、また高い周波数では大気の酸素や水蒸気に吸収されやすい。このため、電波望遠鏡の設置場所としては、標高が高く、水蒸気が少ない場所が適切である。可視光や赤外線など観測する波長により、宇宙空間で異なる現象を捉える事ができるが、電波による宇宙空間の観測では他の波長にはない特徴がある。・可視光では見えないような低温の物体を観測できる。生まれた後の星は可視光を放射するが、星が生まれる前の温度の低い天体は可視光を放射せず、電波を放射している。そのため、このような天体の研究には電波による観測が必要である。・波長が長いこの特徴のため、星間微粒子による吸収を受けにくく、奥の方まで観測することができる。・電気的に干渉技術が容易干渉計と呼ばれる望遠鏡では複数のアンテナを離して置いて観測し、電波を干渉させることにより高い分解能を得ることができるが、電波領域ではこの方法により他の波長による観測よりも高い分解能を得ている。以上のような特徴により、電波による観測は天文学で重要な位置を占めている。

1.3.1 Atacama Large Millimeter Array

1.4 Purpose of this work

Chapter 2

Methylamine survey in Orion-KL

In this chapter, we report the tentatively detection CH_3NH_2 in Orion-KL.

2.1 Observation data

We analyzed 2 ALMA archival data. First we used Cycle 2 data (ADS/JAO.ALMA#2013.1.00553.S, see Pagani et al. (2017)) We also employed the ALMA Science Verification (SV) data (ADS/JAO.ALMA#2011.0.00009.SV) at band 6 to fill up the missing frequency coverage of Cycle 2 data. Details of each session are summarized in Table ??.

The reduced ALMA data cubes of Cycle 2 are available at the CDS via anonymous ftp to cdsarc.u-strasbg.fr (130.79.128.5) or via <http://cdsarc.u-strasbg.fr/viz-bin/qcat?J/A+A/604/A32>. Since the SV data contained not only line emission but continuum emission, we subtracted continuum emission statistically by the method described in Section 2.2.1.

※観測諸元 ×2

2.2 Analysis

2.2.1 Continuum Subtraction of SV data

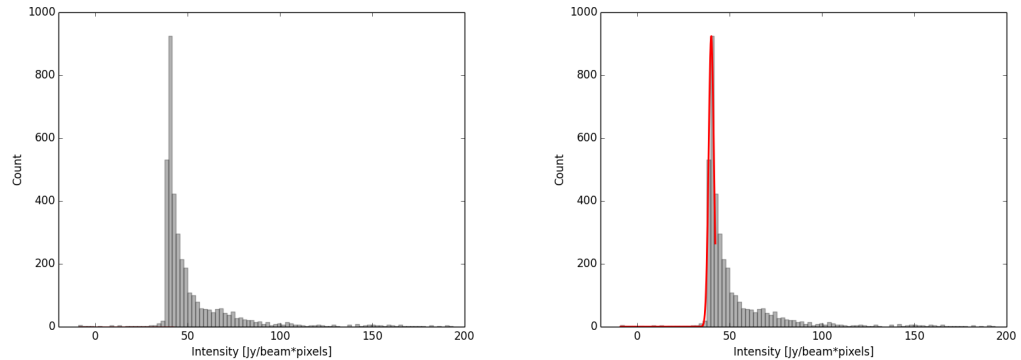


Figure 2.1: Histogram

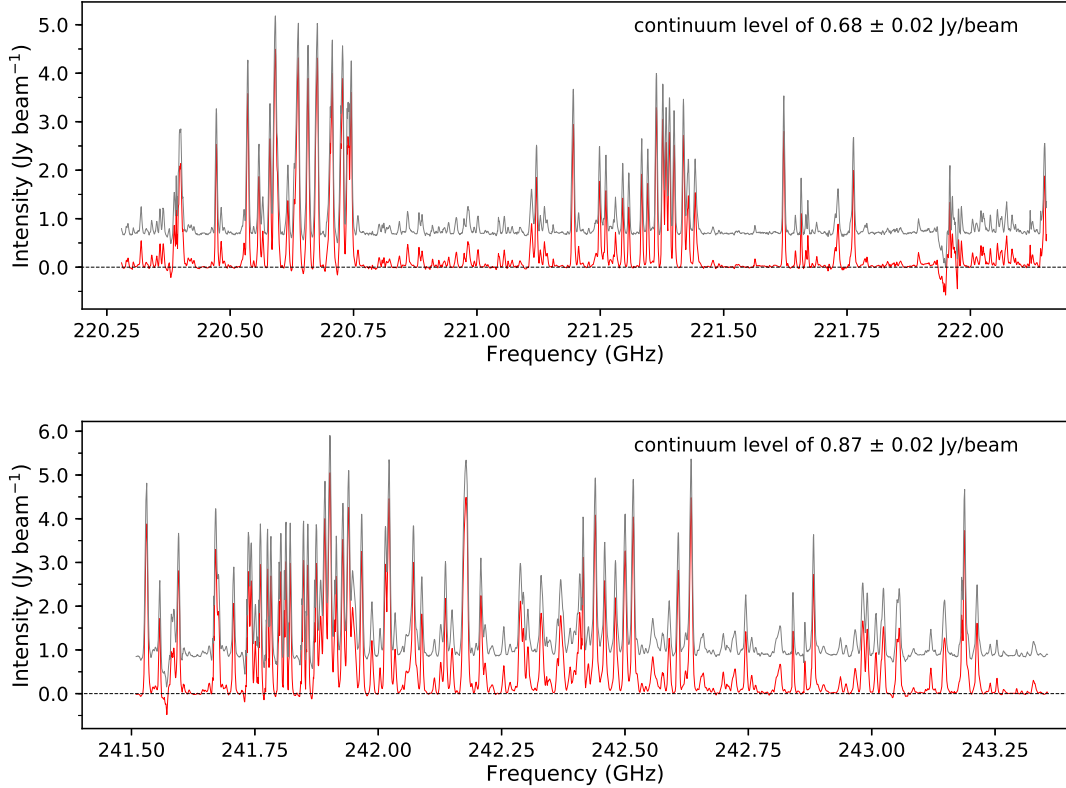


Figure 2.2: The original spectra (gray) and continuum-subtracted spectra (red) towards Hot core. The continuum emission level subtracted to the original spectra, together with its uncertainty, is listed in the upper right part of each panel.

2.2.2 Line identification

We drew CH_3NH_2 emission maps using Common Astronomy Software Applications (CASA) software (McMullin et al., 2007). We used JPL Molecular Spectroscopy catalog to identify the transition lines. 8 spectral features exhibit a compact emission at the center of the Hot core . We extracted spectrum from this region.

2. We estimated the systemic velocity and the line width of 217.758 GHz line, reported by Pagani et al. (2017), which seem contaminated by other lines.
3. Using these value, we obtained the integrated intensity of 8 transitions described in Table 2.1 by Gaussian fitting.

2.3 Results

2.3.1 Transitions

The data obtained for CH₃NH₂ are summarized in Table 2.1. Here the rest frequencies, $S\mu^2$, upper state energy (E_u), the quantum numbers, noise level, and peak brightness temperature are given. Out of 32 predicted transitions ($S\mu^2 > 25 \text{ D}^2$ and $E_u < 200 \text{ K}$) in our observational frequency range, 8 were probably identified in this data set, and are reported in Table 2.1. The remaining 16 CH₃NH₂ transitions are blended with or masked by other spectral features, or its signal are below the noise level (See Appendix A).

Table 2.1: Observed rotational transitions of CH₃NH₂ in Orion-KL

Frequency [GHz]	$S\mu^2 [\text{D}^2]$	$E_u [\text{K}]$	Transition (J, K_a, Γ)	Noise [K]	peak $T_B [K]$	Comments
215.670	53.92	111.48	9, 2, $E_{1-1} \rightarrow 9, 1, E_{1+1}$			
245.202	37.84	168.31	12, 1, $B_2 \rightarrow 11, 2, B_1$			Reported in Pagani+17
217.758	129.88	182.05	12, 2, $B_2 \rightarrow 12, 1, B_1$			Reported in Pagani+17
221.755	35.06	133.11	10, 2, $A_2 \rightarrow 10, 1, A_1$			SV data
229.908	27.37	92.71	8, 2, $A_2 \rightarrow 8, 1, A_1$			
235.735	82.06	92.76	8, 2, $B_2 \rightarrow 8, 1, B_1$			Reported in Pagani+17
242.262	60.23	60.86	6, 2, $B_2 \rightarrow 6, 1, B_1$			SV data
244.887	49.54	48.09	5, 2, $B_1 \rightarrow 5, 1, B_2$			Reported in Pagani+17

2.3.2 Distribution

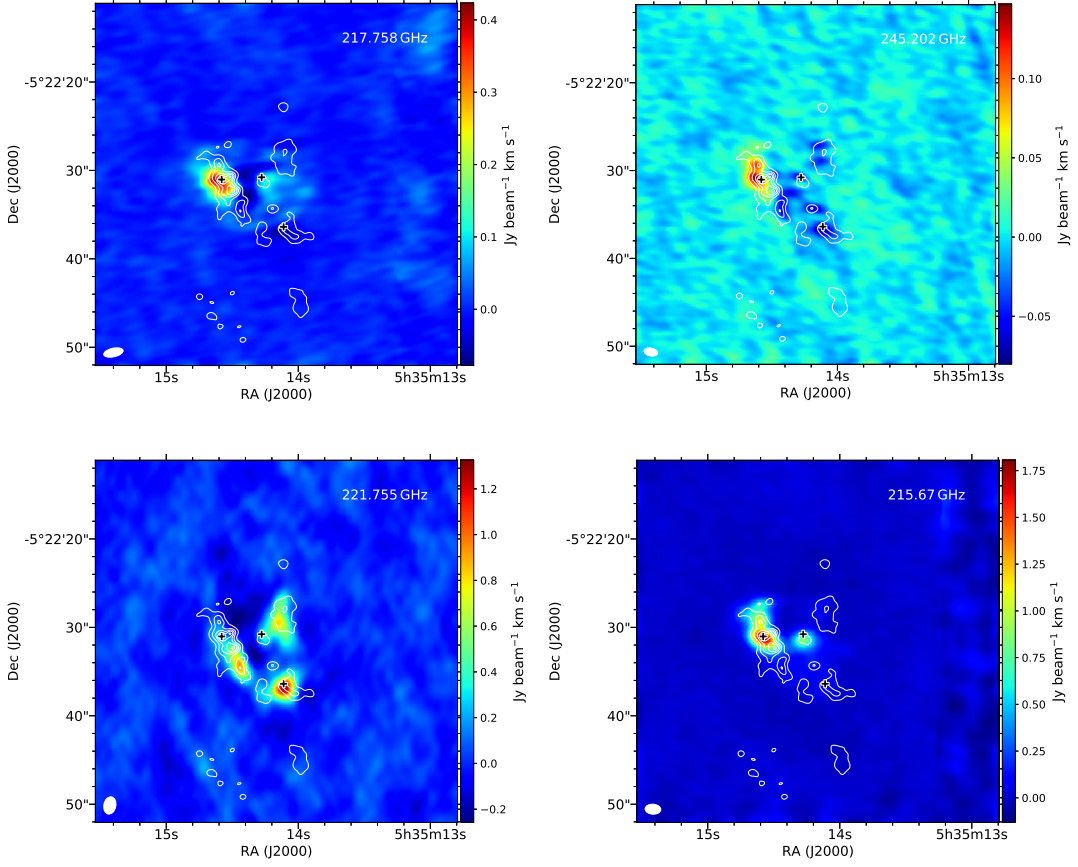


Figure 2.3: Integrated intensity maps of unblended CH_3NH_2 lines. The white contours show the 1.3 mm continuum map from Hirota et al. (2015), where the contour levels are 10 %, 30 %, 50 %, 70 %, 90 % of the peak intensity. Black crosses denote Hot core, IRC7, and Compact ridge. The rest frequency of each transition shows in the upper right part of each panel.

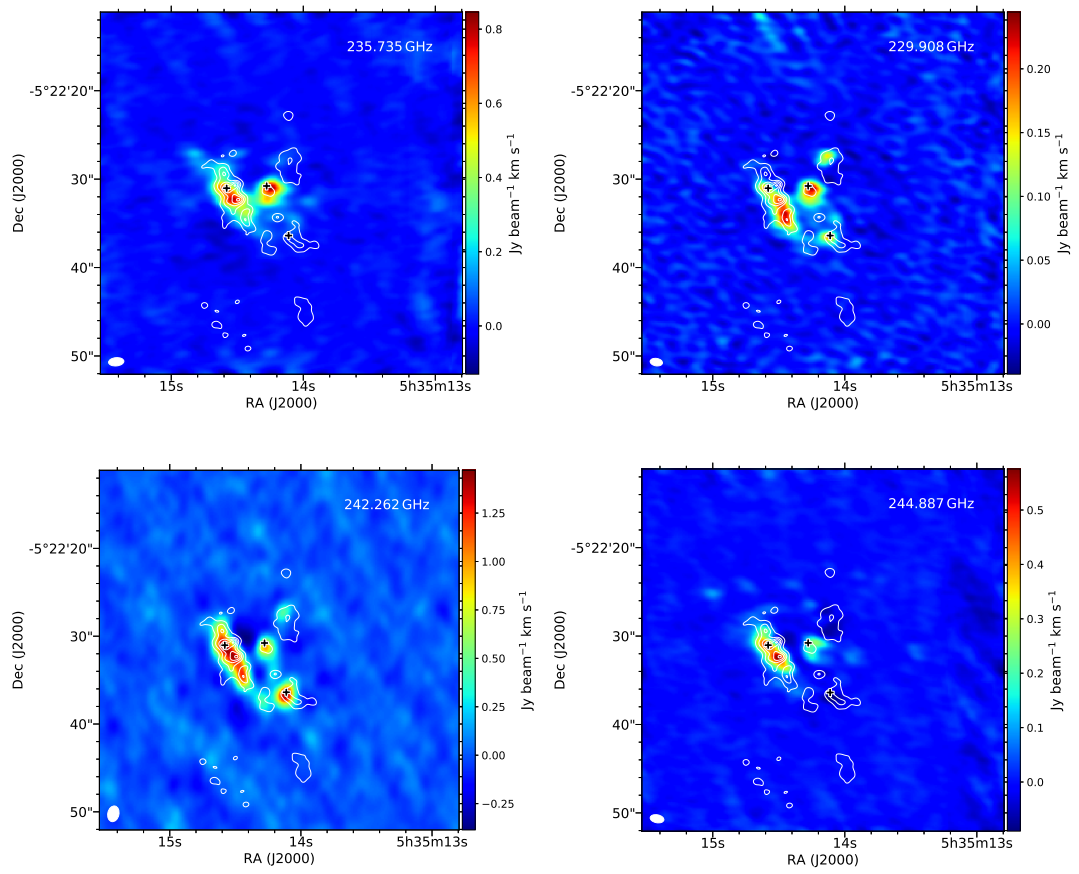


Figure 2.4: (Continued)

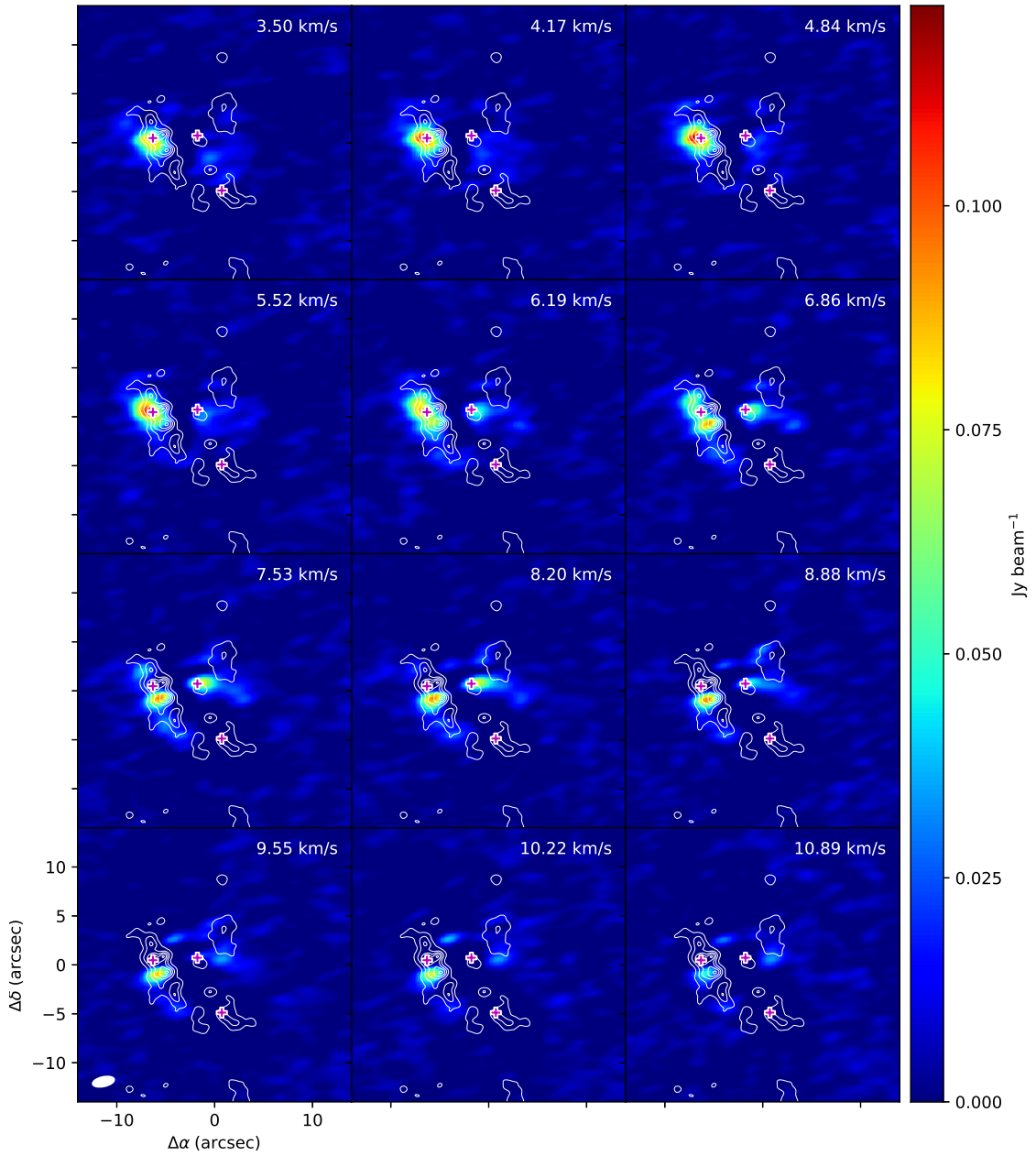


Figure 2.5: Channel map of expected unblended 217.758 GHz line show multiple velocity-dependent emission peaks: $4\text{-}6 \text{ km s}^{-1}$ towards Hot core, $7\text{-}9 \text{ km s}^{-1}$ towards IRc7. Magenta crosses denote Hot core, IRc7, and Compact ridge.

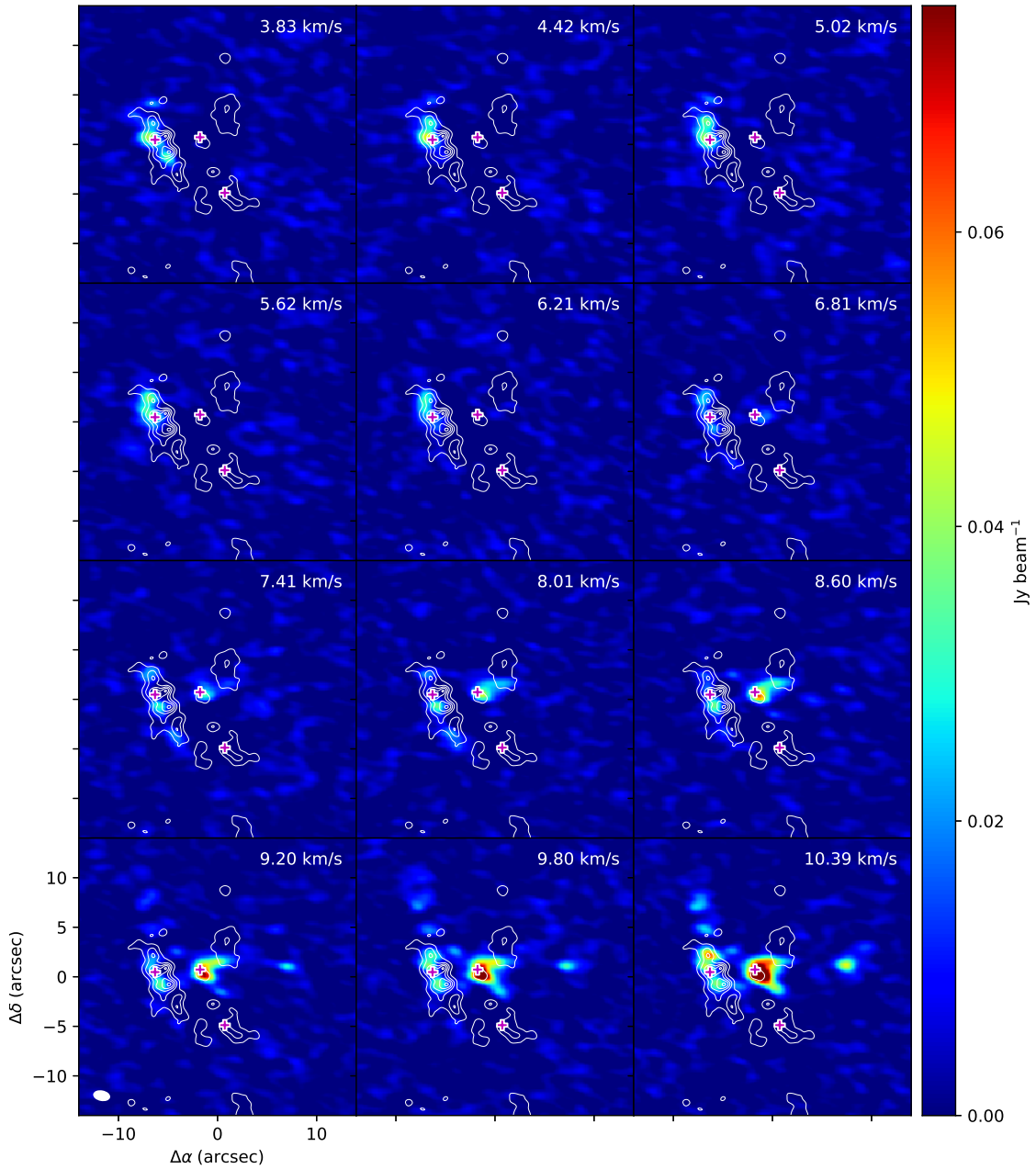


Figure 2.6: Channel map of expected unblended 245.202 GHz line.

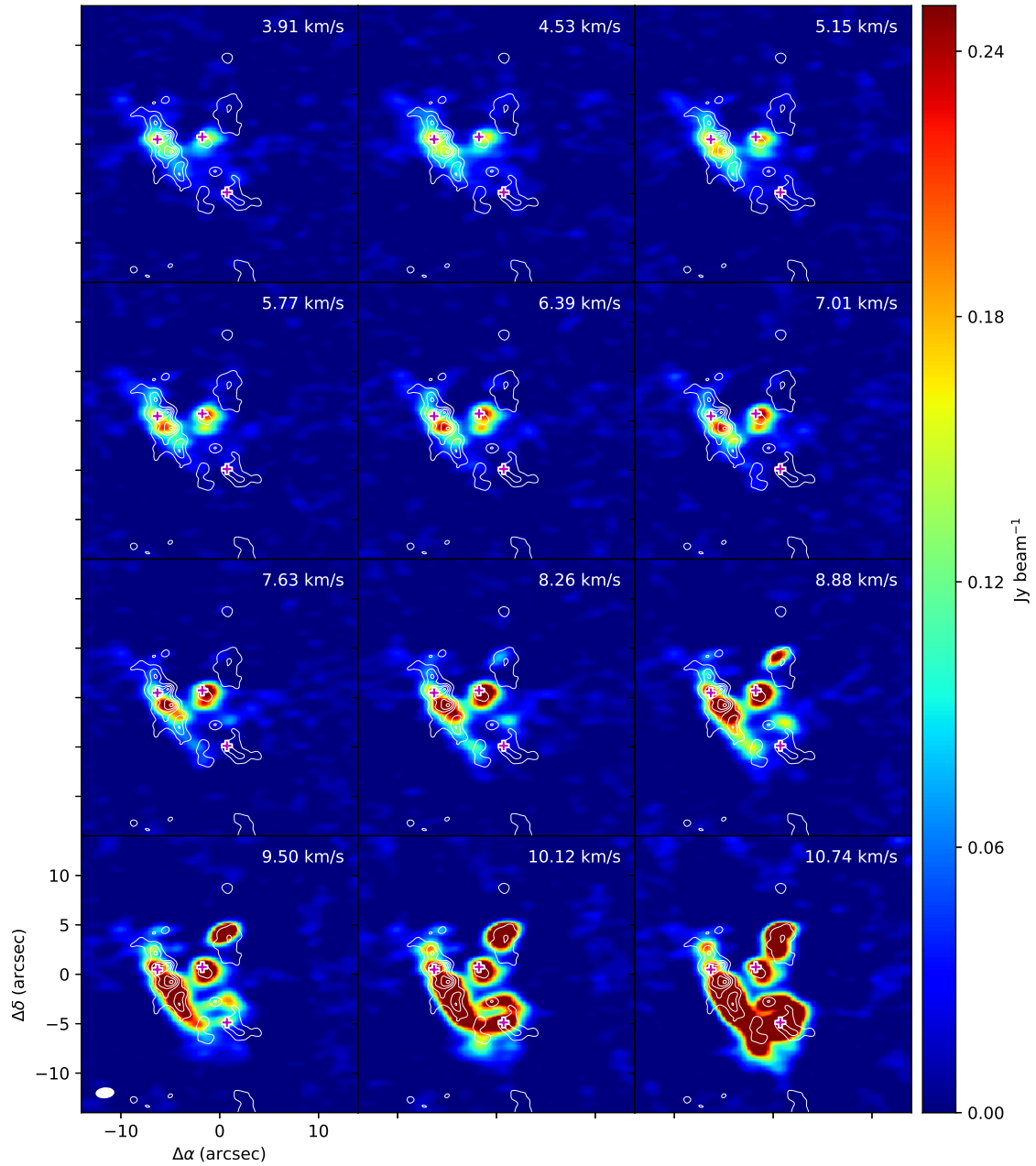


Figure 2.7: Channel map of expected unblended 235.735 GHz line.

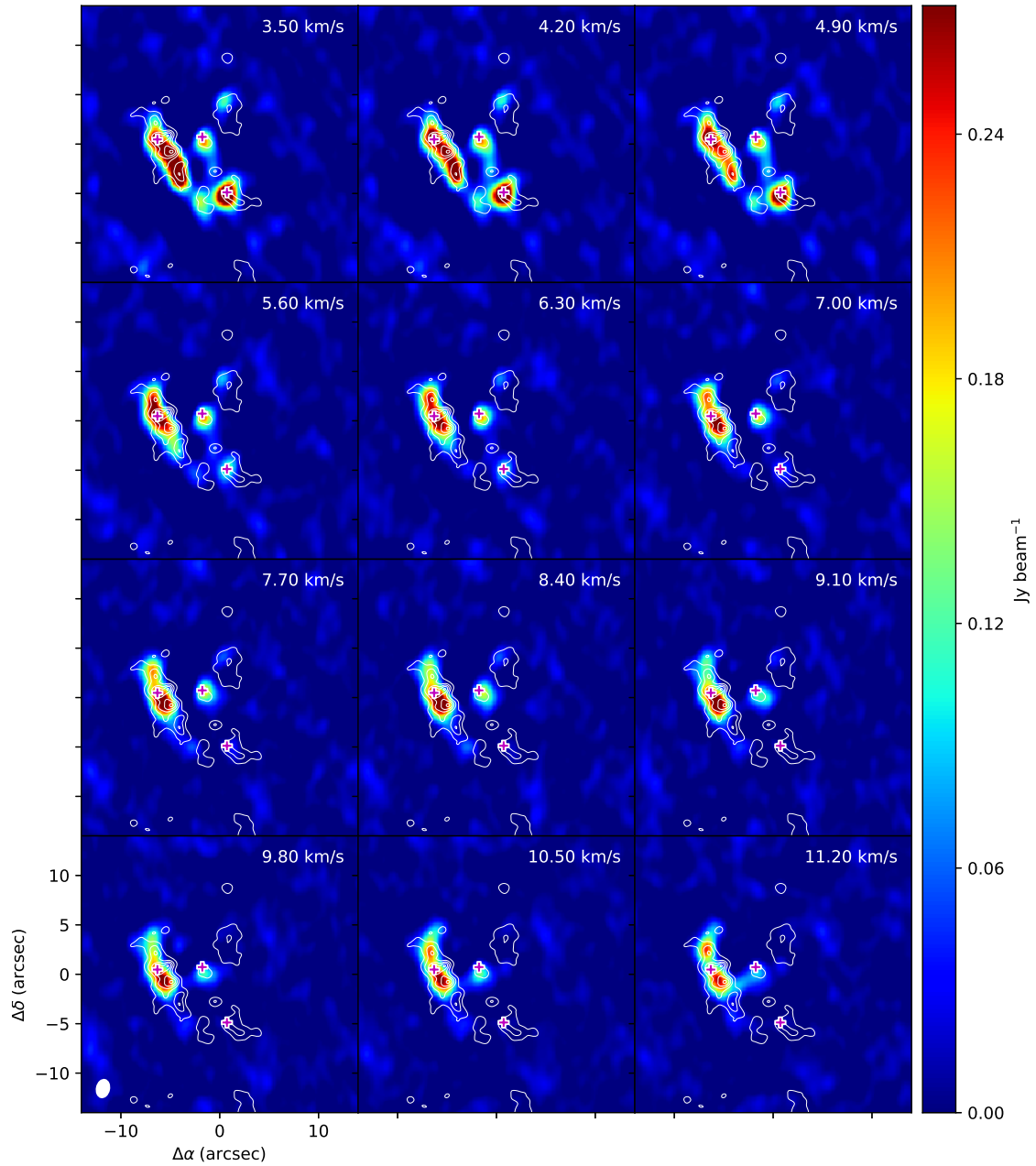


Figure 2.8: Channel map of expected unblended 242.262 GHz line.

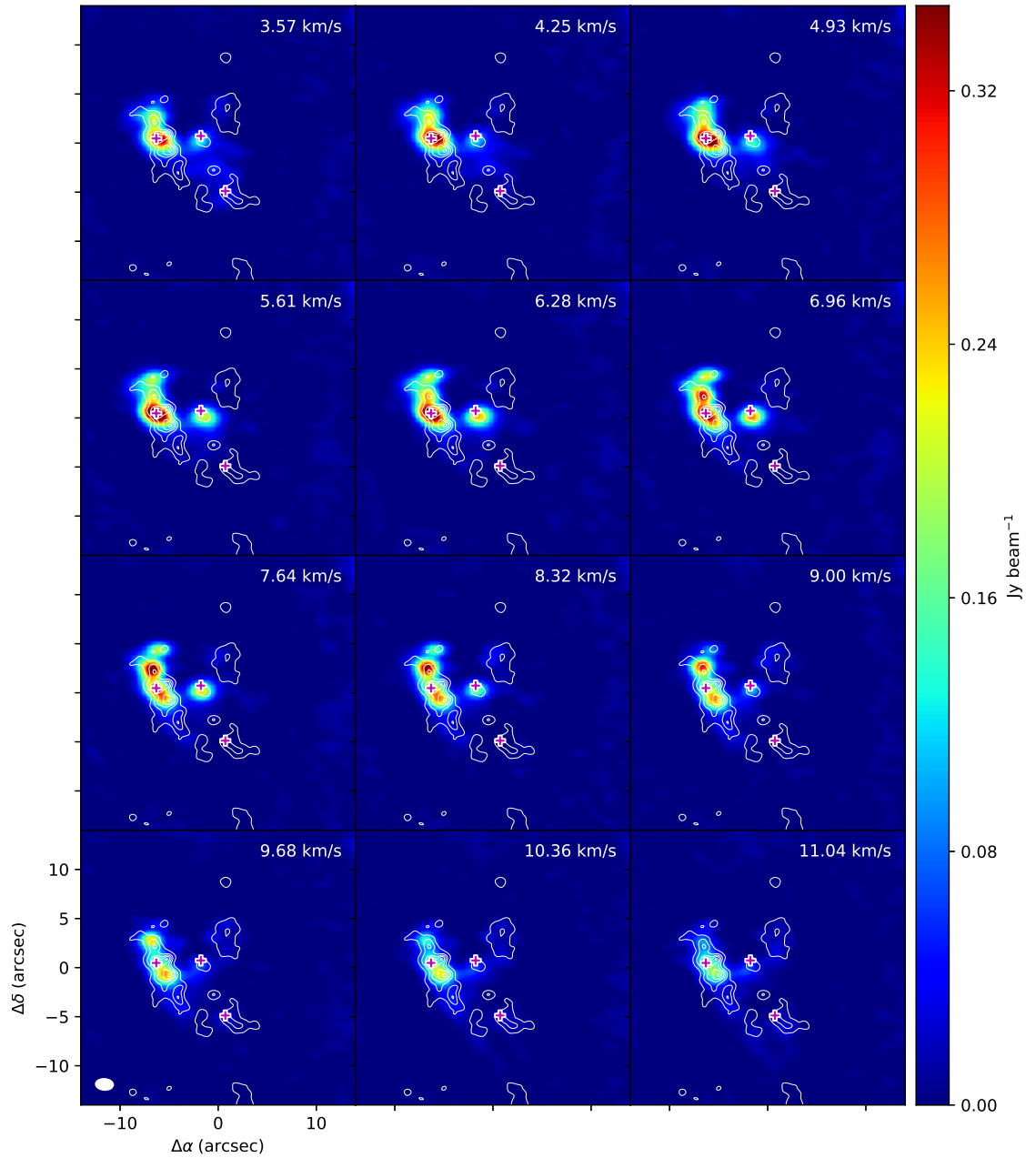


Figure 2.9: Channel map of expected unblended 215.670 GHz line.

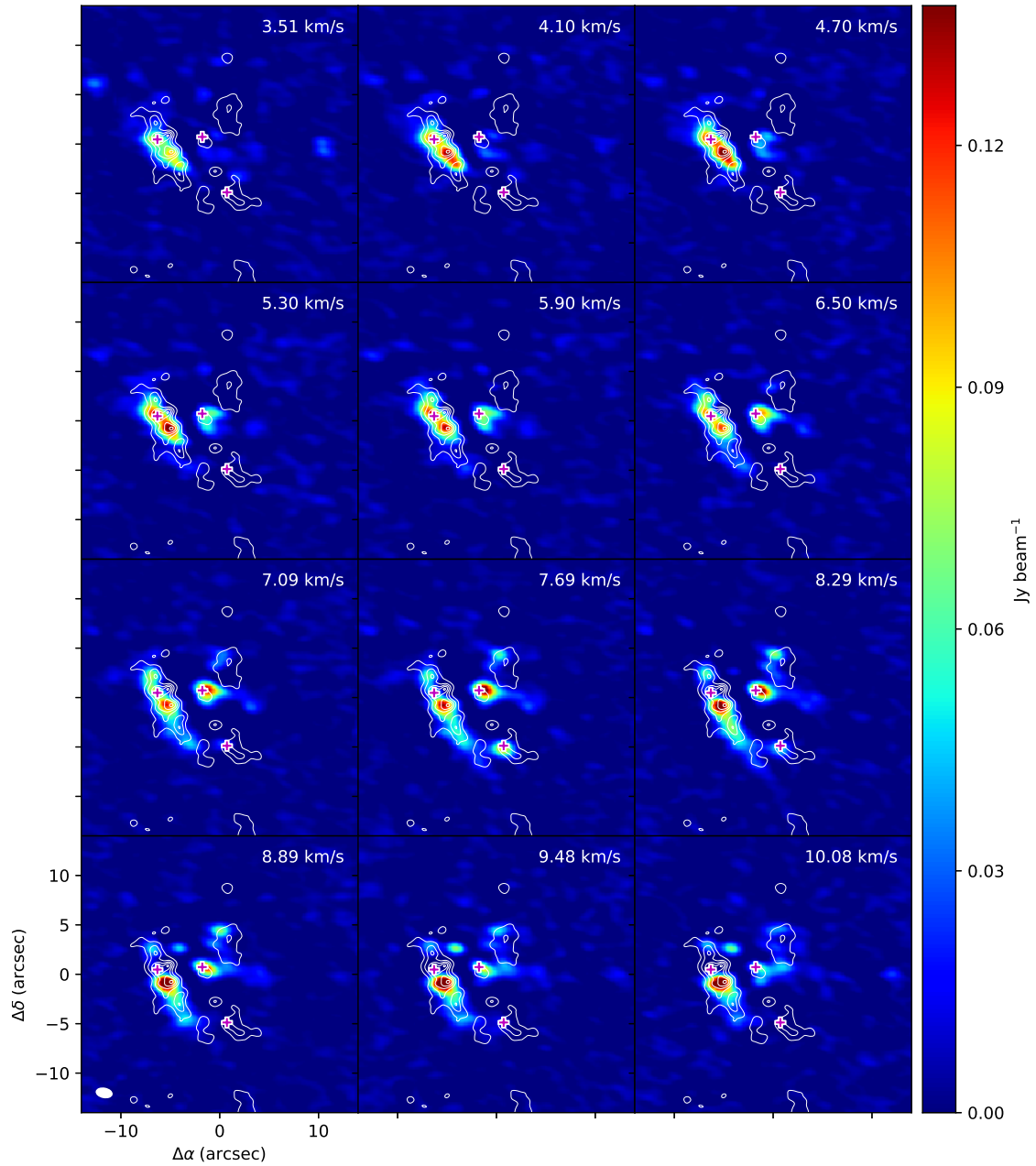


Figure 2.10: Channel map of expected unblended 244.887 GHz line.

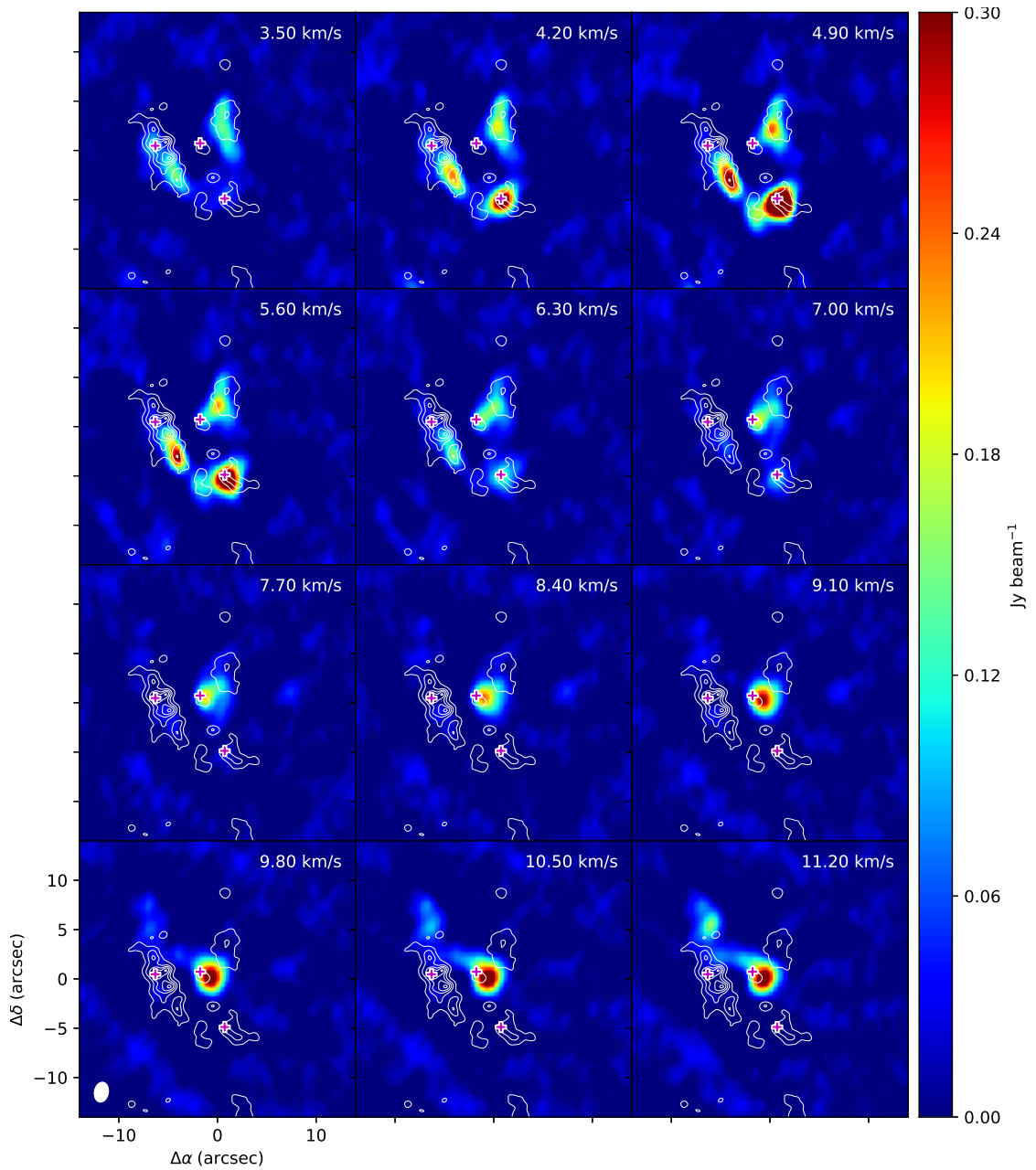


Figure 2.11: Channel map of expected unblended 221.755 GHz line.

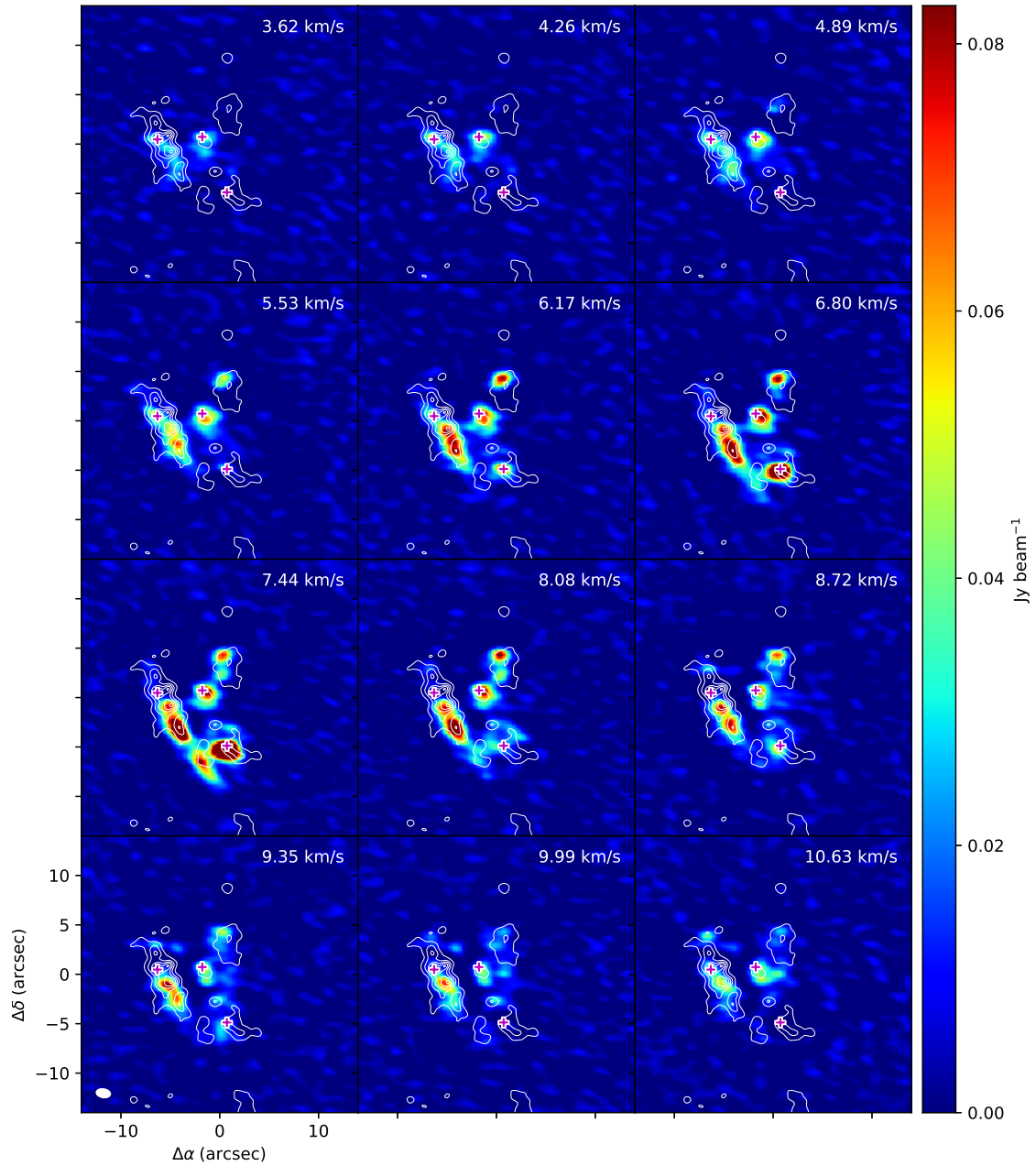


Figure 2.12: Channel map of expected unblended 229.908 GHz line.

2.3.3 Spectrum

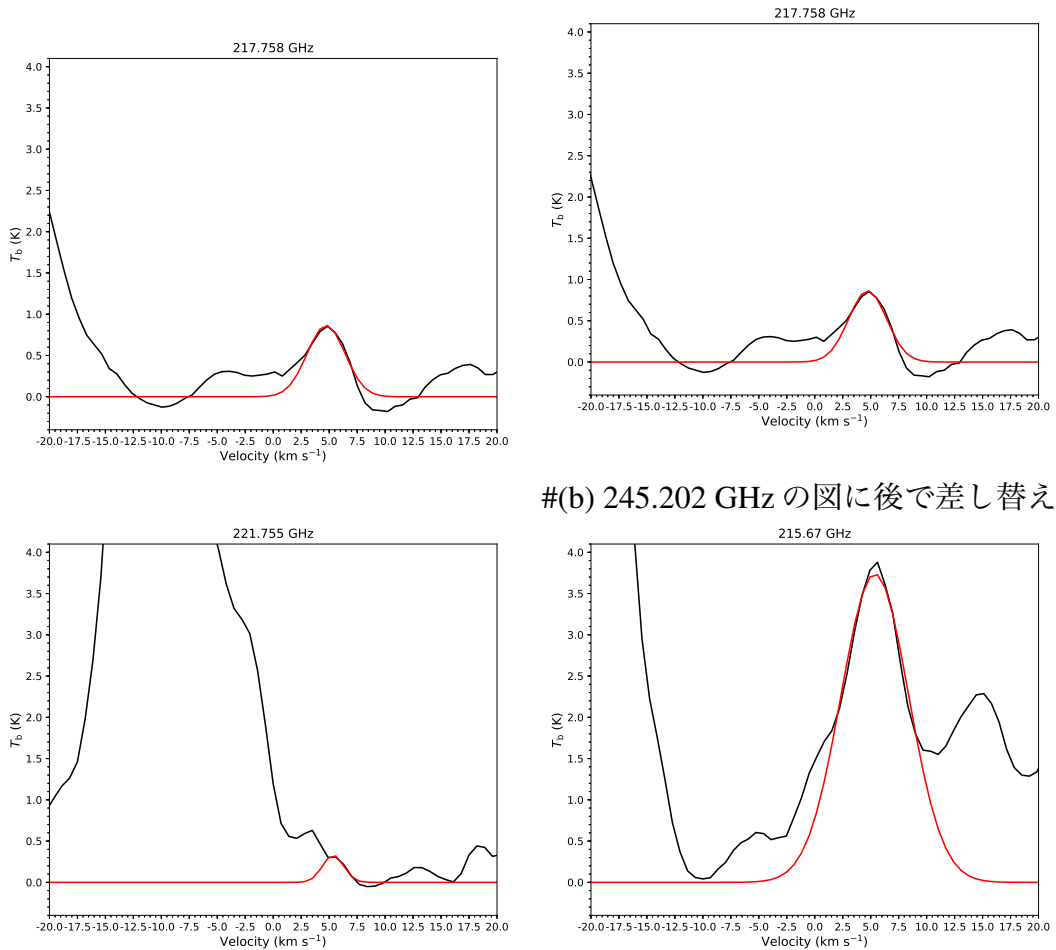


Figure 2.13: Spectrum of

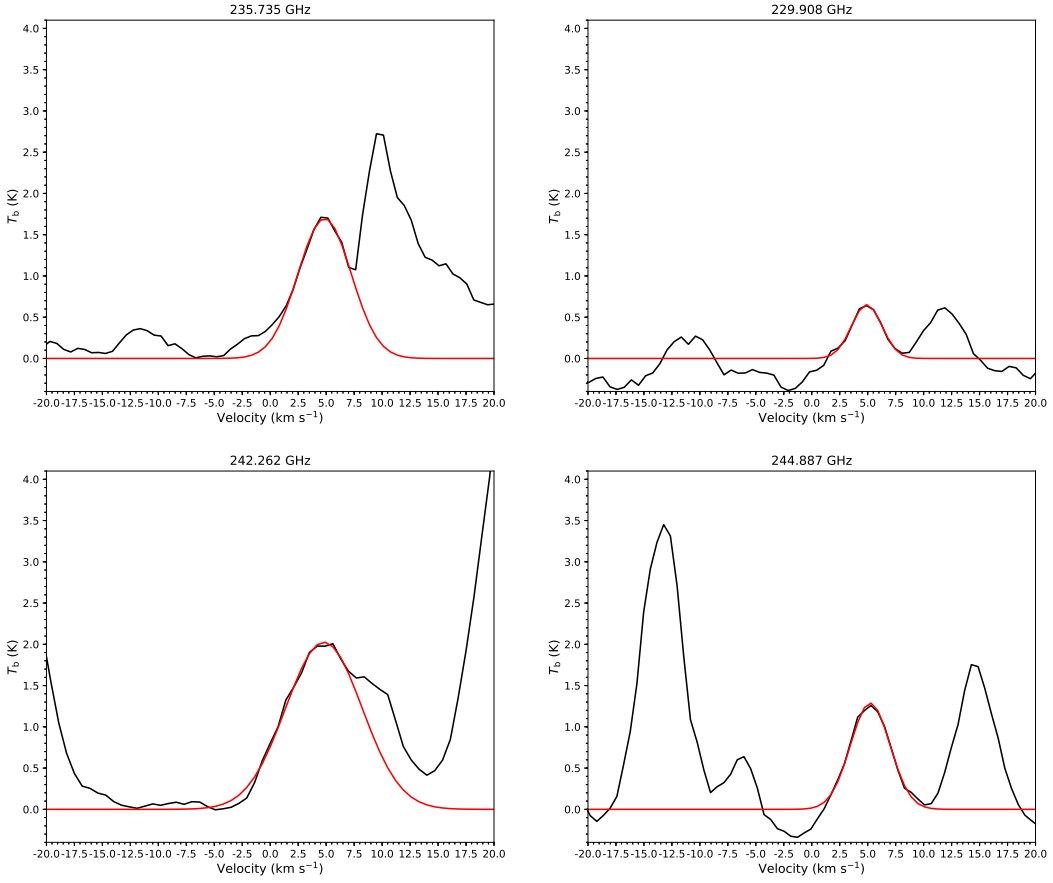


Figure 2.14: (Continued)

2.4 Disucssion

2.4.1 Column density and Rotation temperature

In this subsection we will describe the methodologies in deriving fractional abundances of COMs. The column density of CH_3NH_2 (N_{MA}) was established by using the rotational temperature diagram method, which assumes local thermodynamic equilibrium (LTE) and optically thin emission. The following equation was employed for the analysis (Turner, 1991):

$$\log \frac{3 k_{\text{B}} T_{\text{B}} \Delta V_{1/2}}{8 \pi^3 \nu S \mu_0^2} = \log \frac{N_{\text{MA}}}{U_{\text{rot}}} - \frac{E_{\text{u}}}{k_{\text{B}}} \frac{\log e}{T_{\text{rot}}} \quad (2.1)$$

In the expression, ν is the rest frequency of the transition, μ_0 is the permanent dipole moment, U_{rot} is the rotational partition function, S is the line strength, E_u is the upper state energy, and T_B and $\Delta V_{1/2}$ are the brightness temperature and line widths (FWHM, in km s^{-1}), respectively. We assumed $\Delta V_{1/2} = 4.24 \text{ km s}^{-1}$, which derived by the Gaussian fitting for 217.758 GHz line.

The brightness temperature can be converted from intensity I_ν when the Rayleigh-Jeans law is applicable.

$$T_B = \frac{c^2}{2 k_B \nu^2} I_\nu \quad (2.2)$$

※ RD の図が完成したら追記する※

The resulting plots are given in Figure ???. The analysis yields a rotational temperature of $T_{\text{rot}} = 93.3 \pm 43.2 \text{ K}$, with a column density of $N_{\text{MA}} = (5.5^{+9.3}_{-3.4}) \times 10^{14} \text{ cm}^{-2}$.

2.4.2 Blending

As shown in Figure ???, the CH_3NH_2 data produced point-to-point scatter perhaps because of the lower signal-to-noise ratio for the weaker transitions in SV data and possible low-level contamination.

Chapter 3

Methylamine survey in low mass star-forming regions

3.1 Review of low mass star-forming region

3.2 Analysis

3.3 IRAS 16293

3.3.1 Observation data

3.3.2 Results

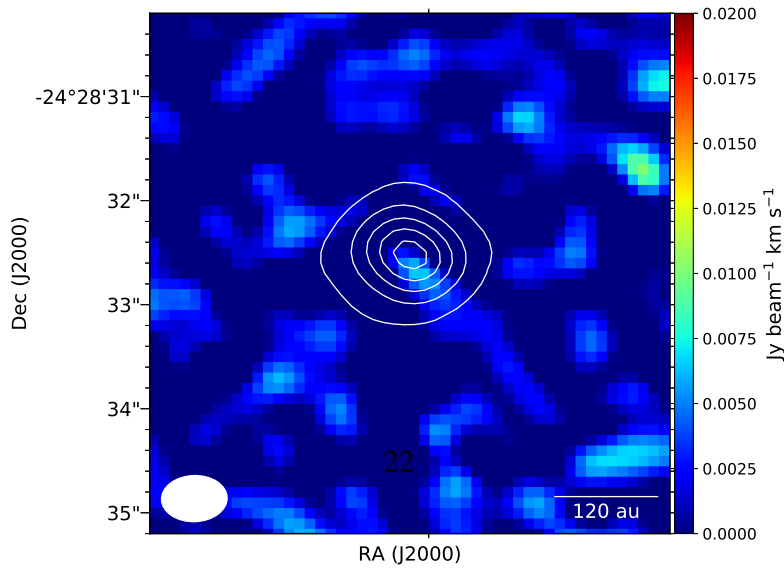


Figure 3.1: Integrated intensity map around 247.362 GHz. The white contours represent

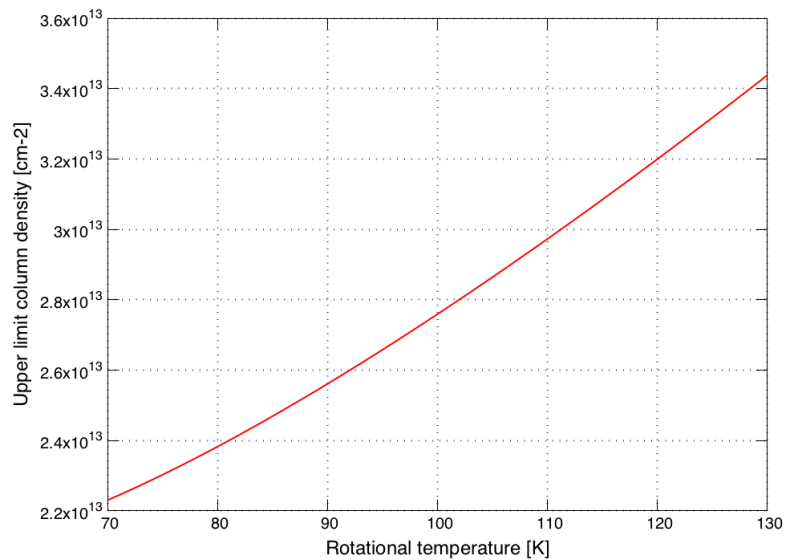


Figure 3.2: Upper limit column density for the strongest CH_3NH_2 transition ($7_2E_{1-1} \rightarrow 7_1E_{1-1}$) as function of T_{rot} . A 3σ value of $11.4 \text{ mJy beam}^{-1}$ is used.

3.4 L483

3.4.1 Observation data

3.4.2 Results

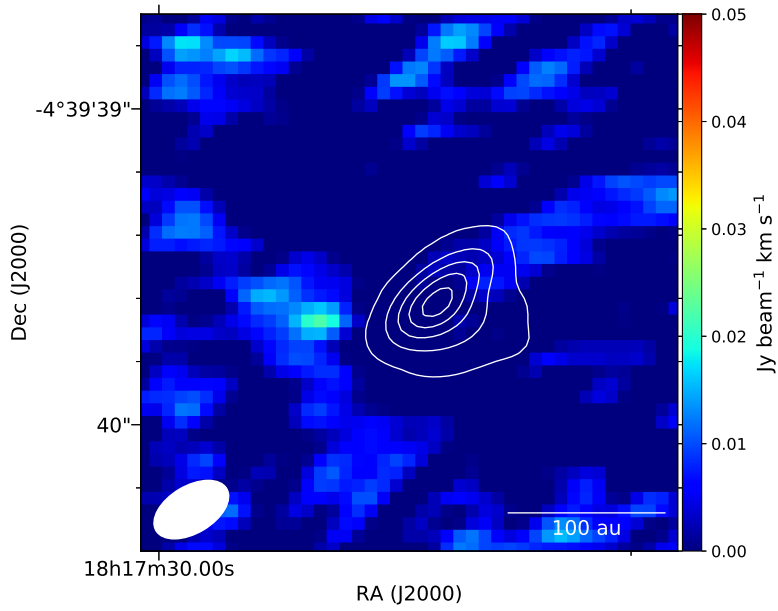


Figure 3.3: Integrated intensity map around 217.079 GHz. The white contours represent the 1.3 mm continuum map, where the contour levels are 10 %, 30 %, 50 %, 70 %, 90 % of the peak intensity.

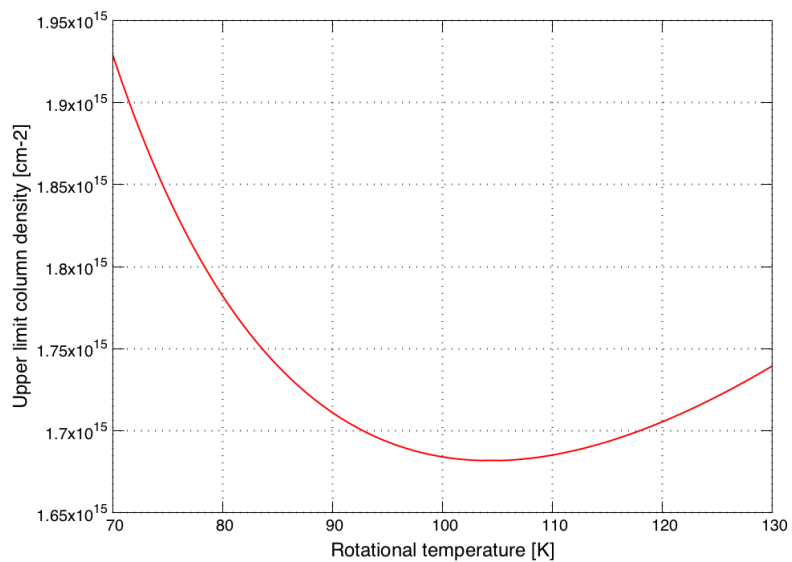


Figure 3.4: Upper limit column density for the strongest CH_3NH_2 transition ($11_2A_1 \rightarrow 11_2A_2$) as function of T_{rot} . A 3σ value of $22.5 \text{ mJy beam}^{-1}$ is used.

Chapter 4

Discussion

Chapter 5

Conclusions

Appendix A

Distribution of methylamine lines contaminated by other molecular line emission in Orion-KL

A.1 Integrated intensity maps

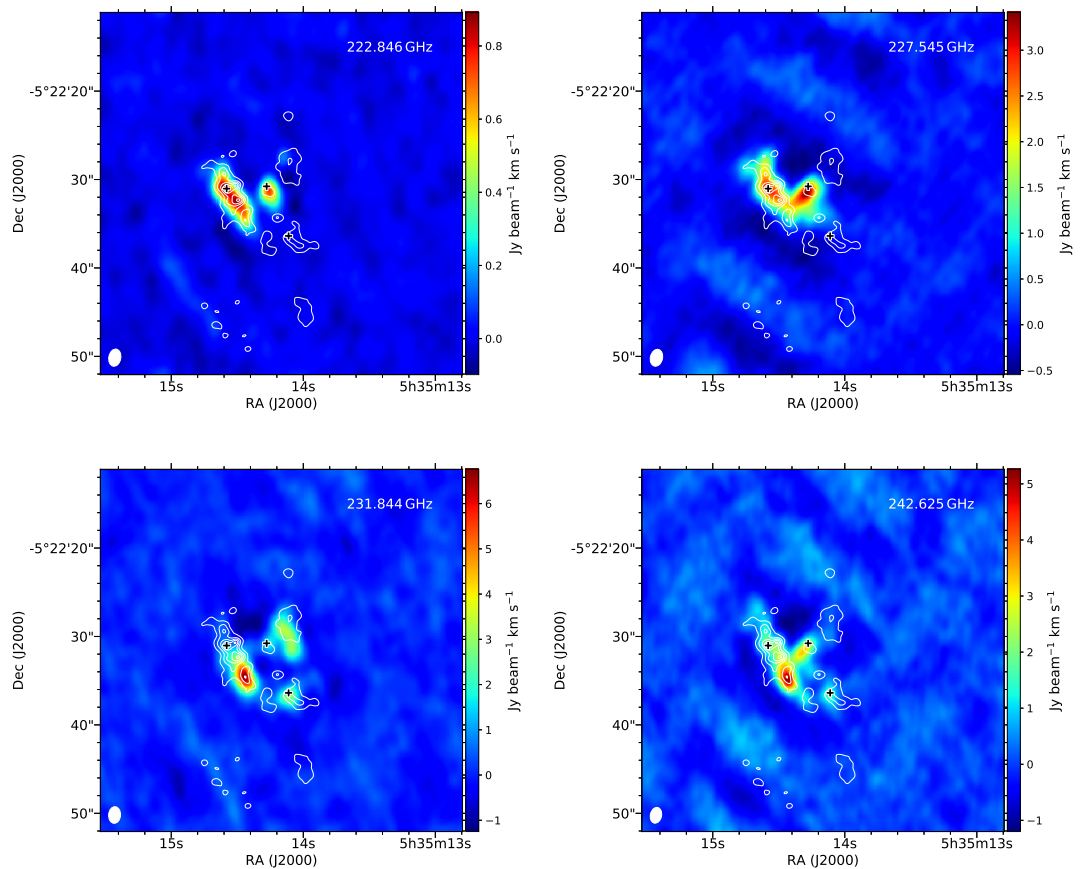


Figure A.1: Integrated intensity maps around methylamine line.

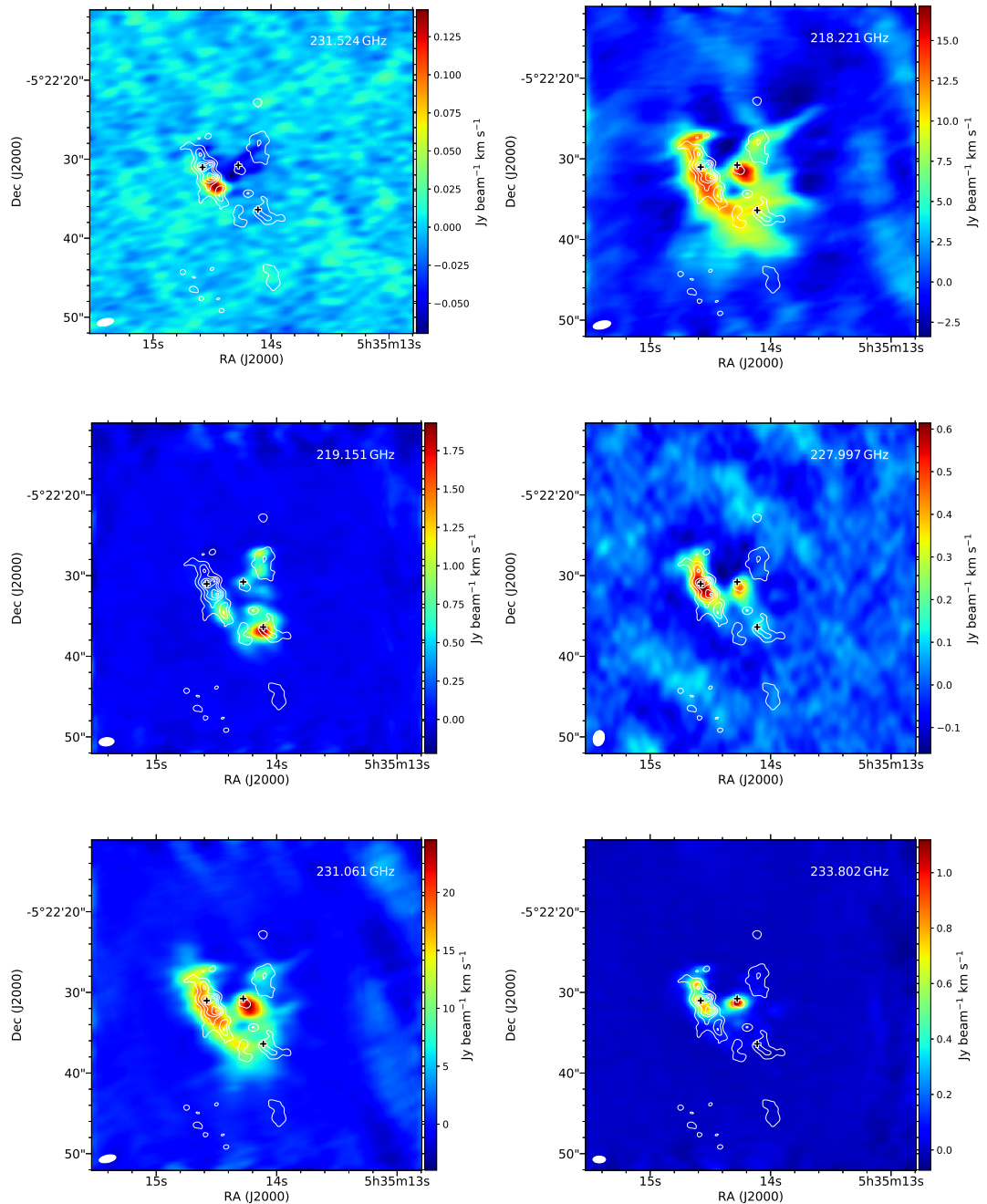


Figure A.2: (Continued)

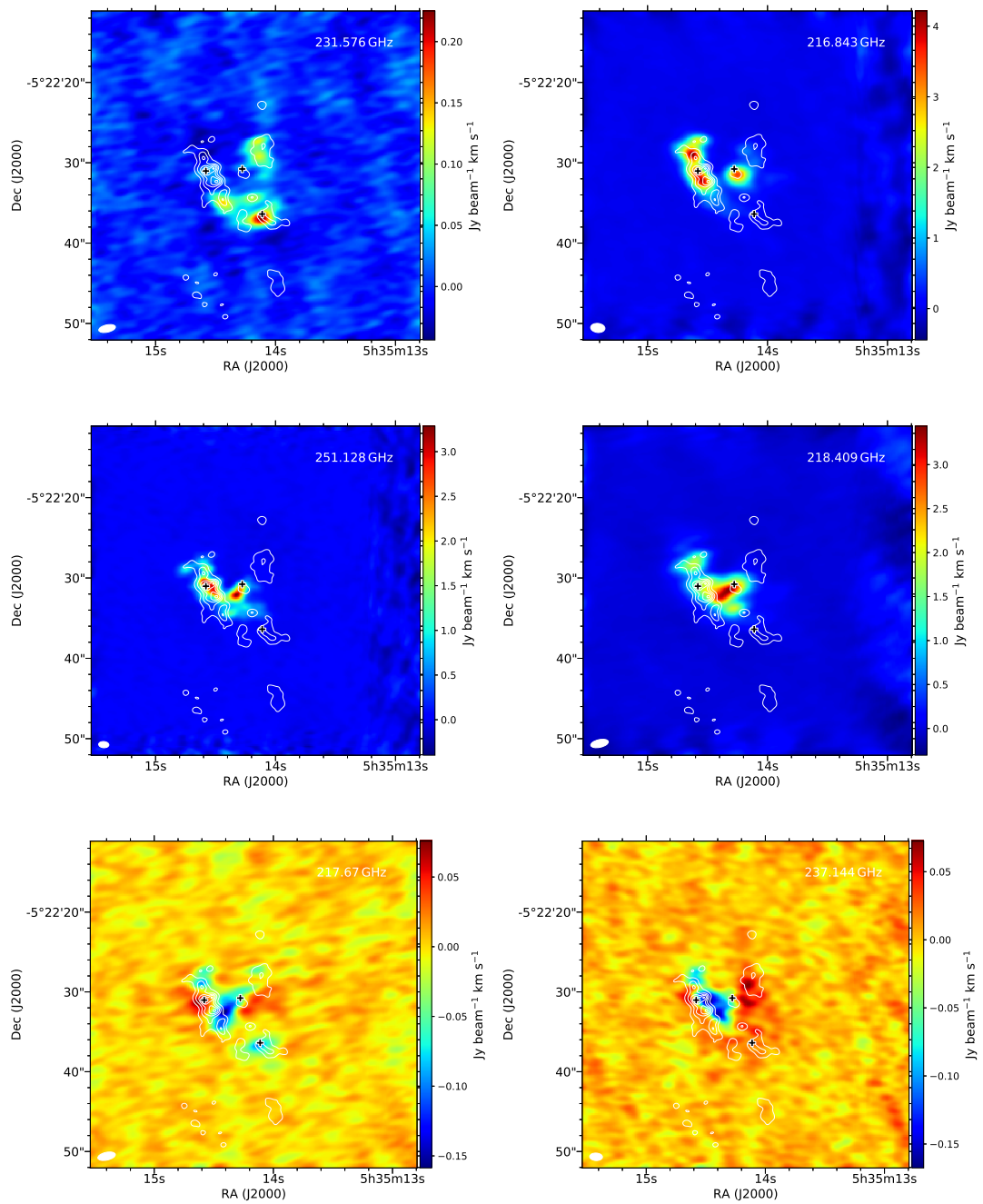


Figure A.3: (Continued)

A.2 Channel maps

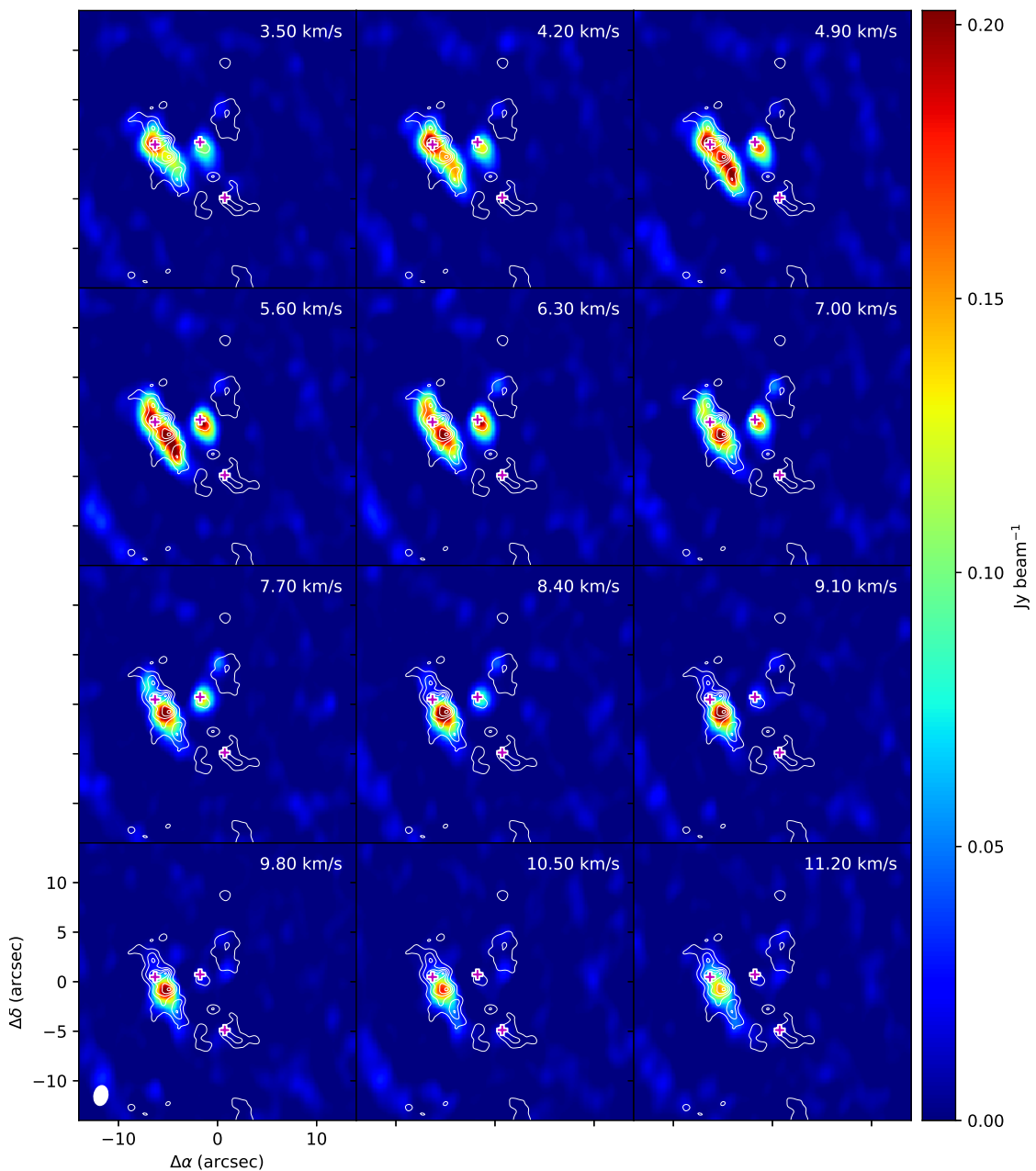


Figure A.4: 222.846GHz

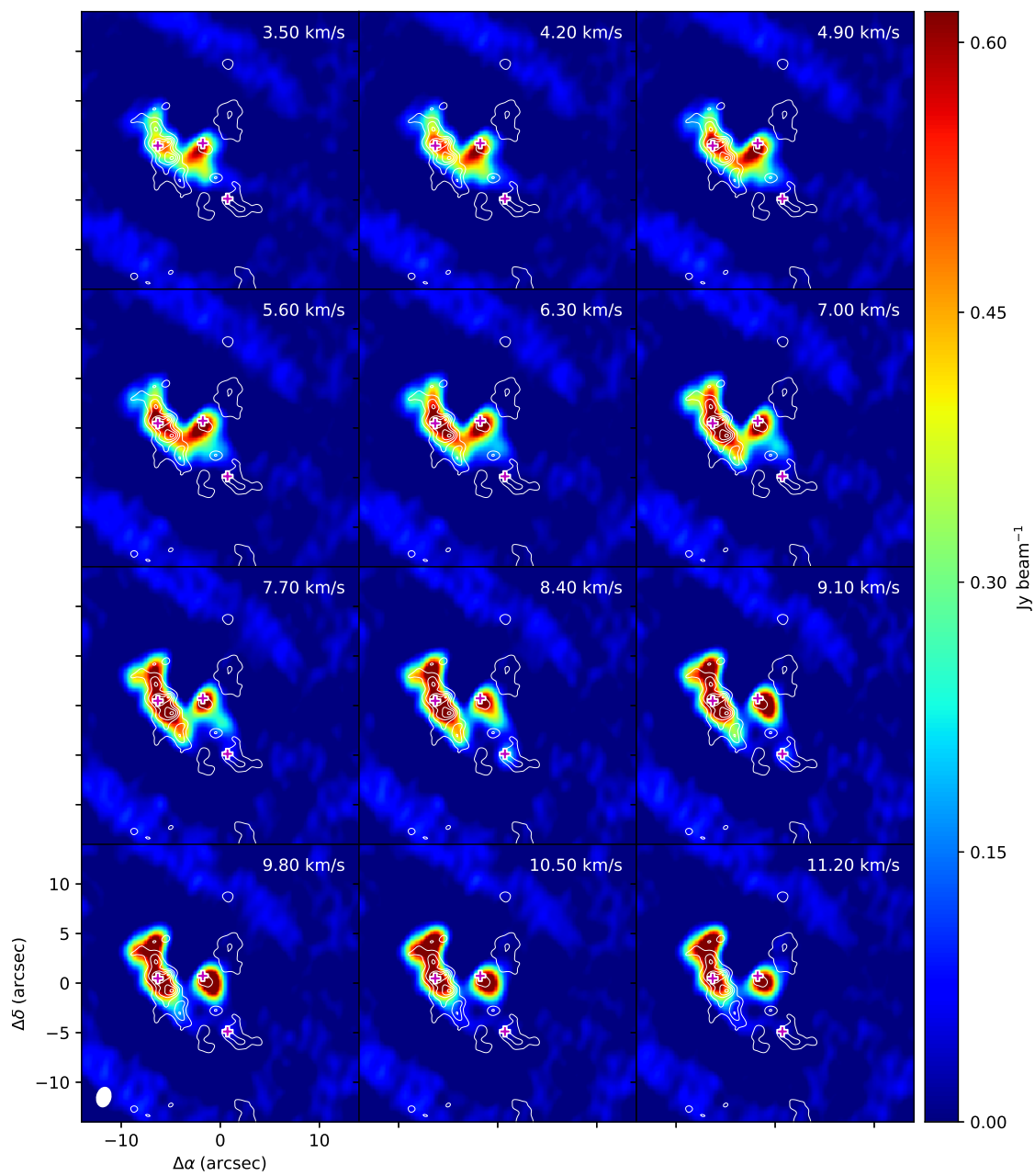


Figure A.5: 227.545GHz

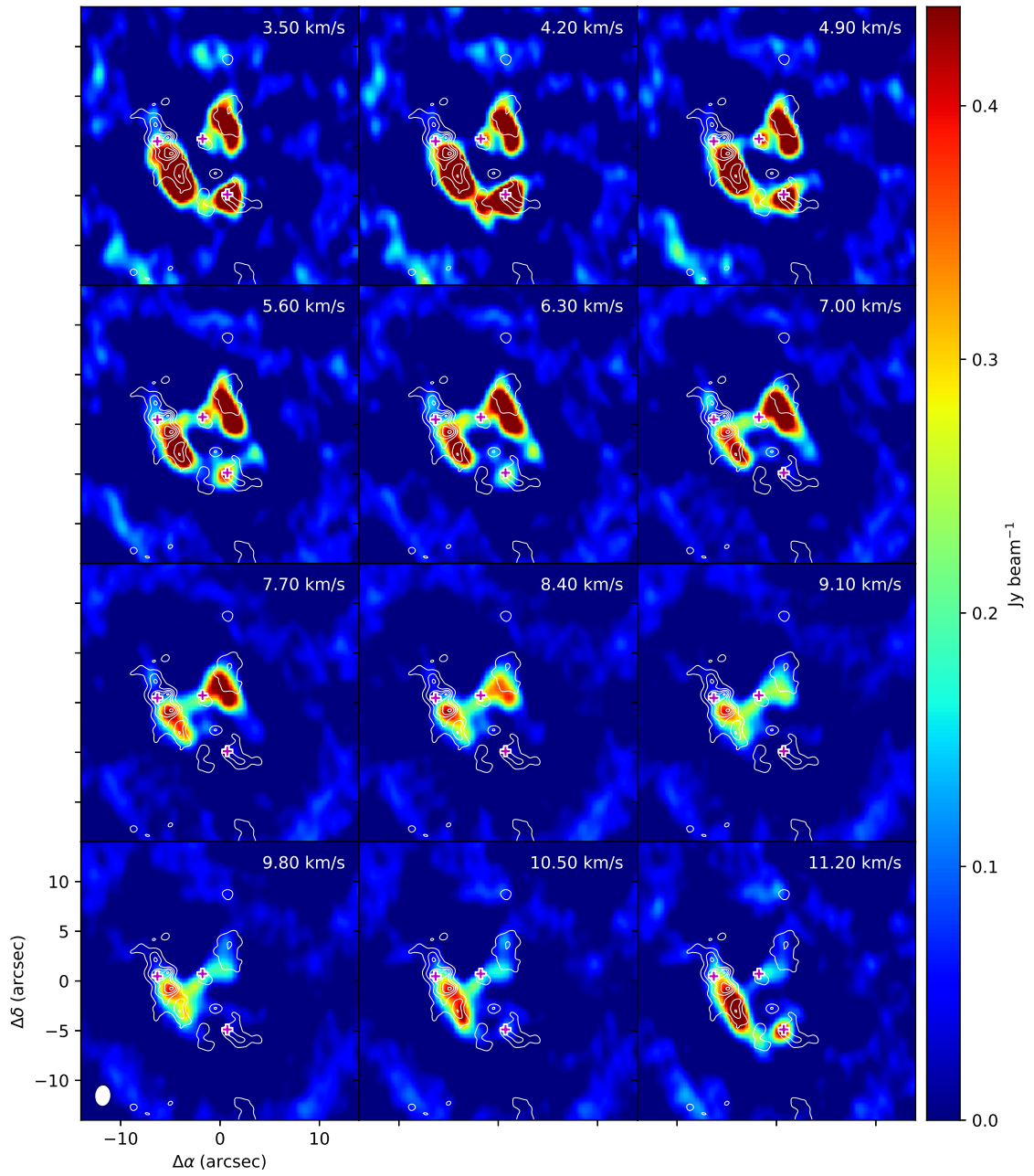


Figure A.6: 231.844GHz

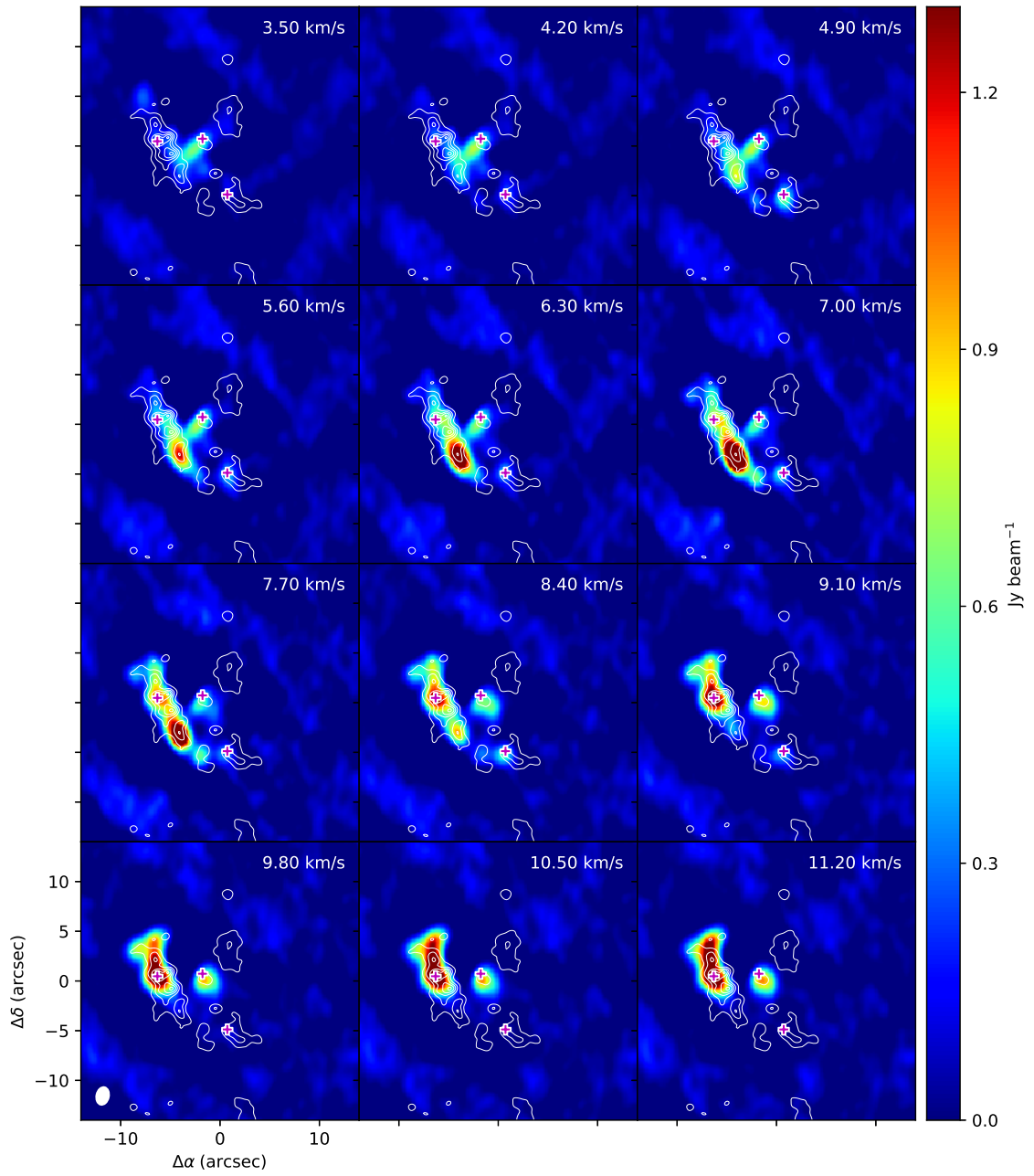


Figure A.7: 242.625GHz

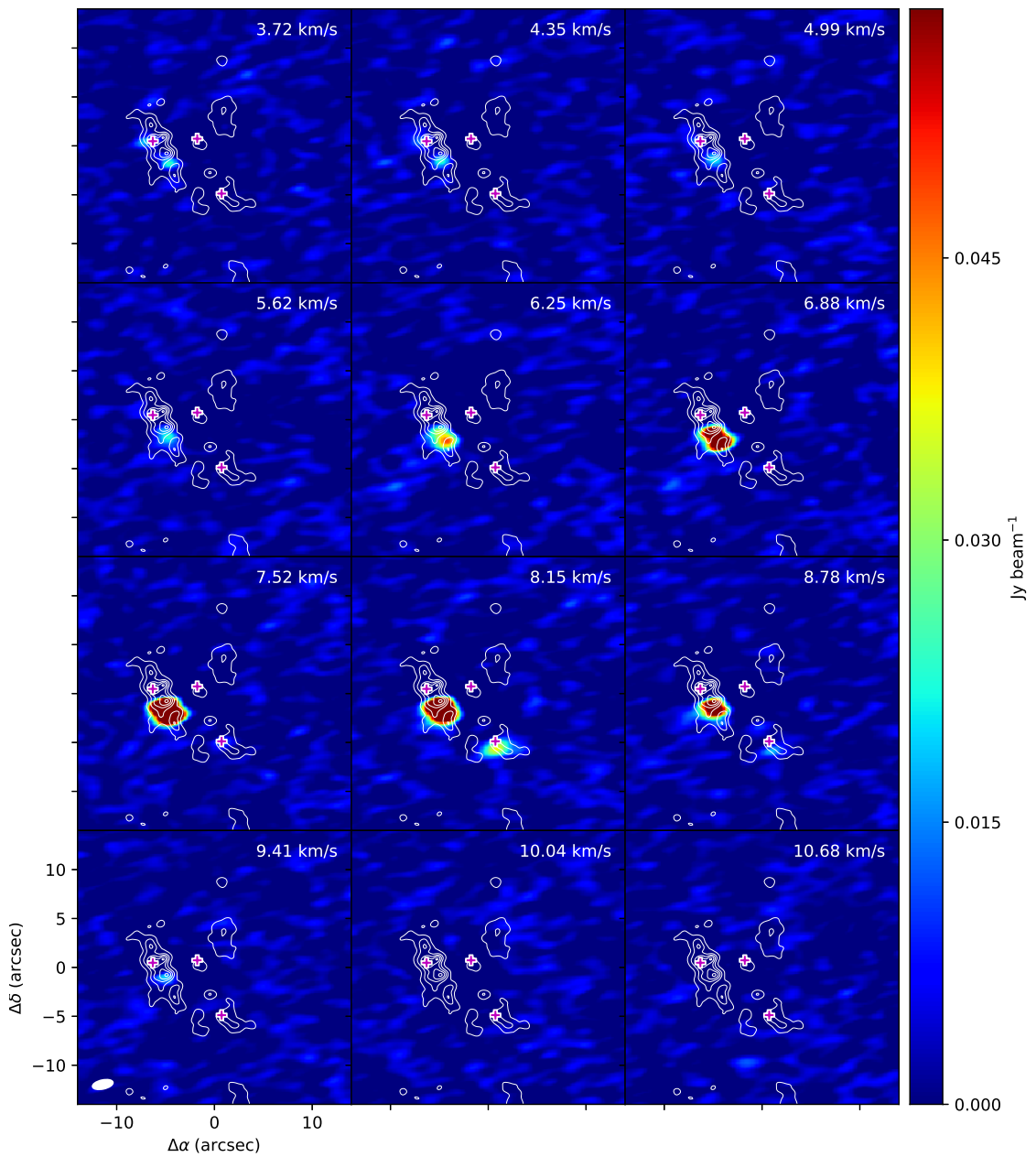


Figure A.8: 231.524GHz

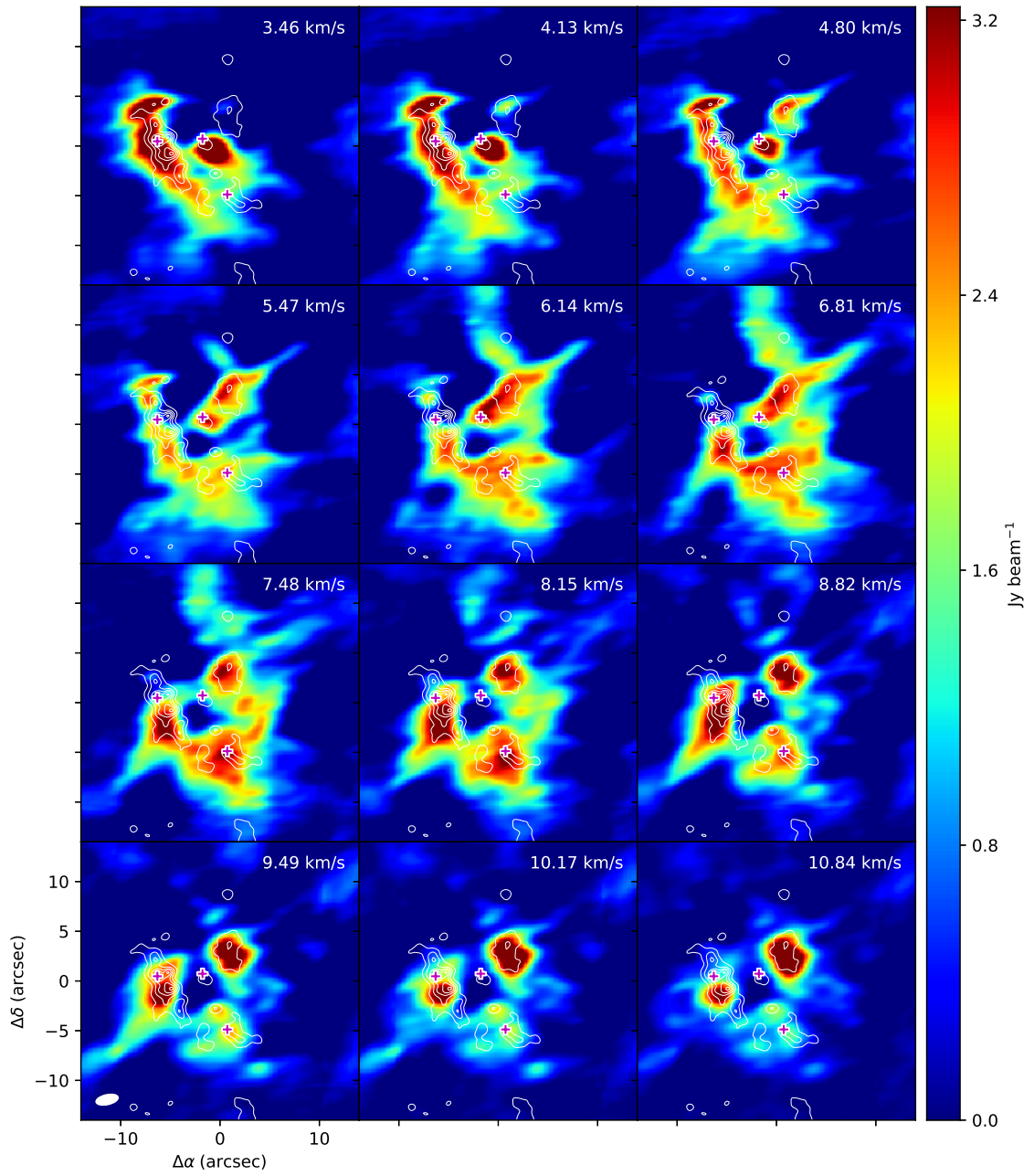


Figure A.9: 218.221GHz

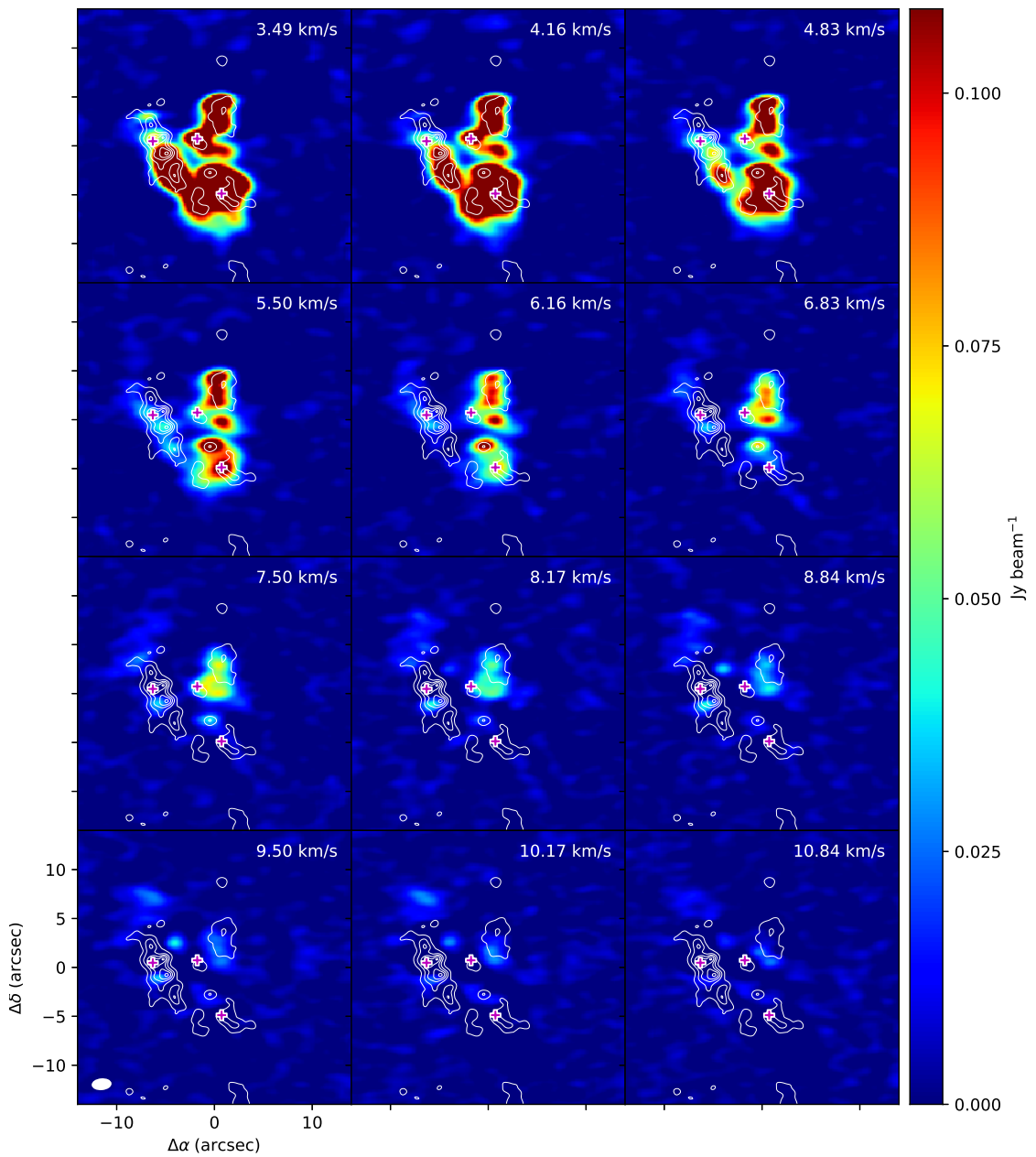


Figure A.10: 219.151GHz

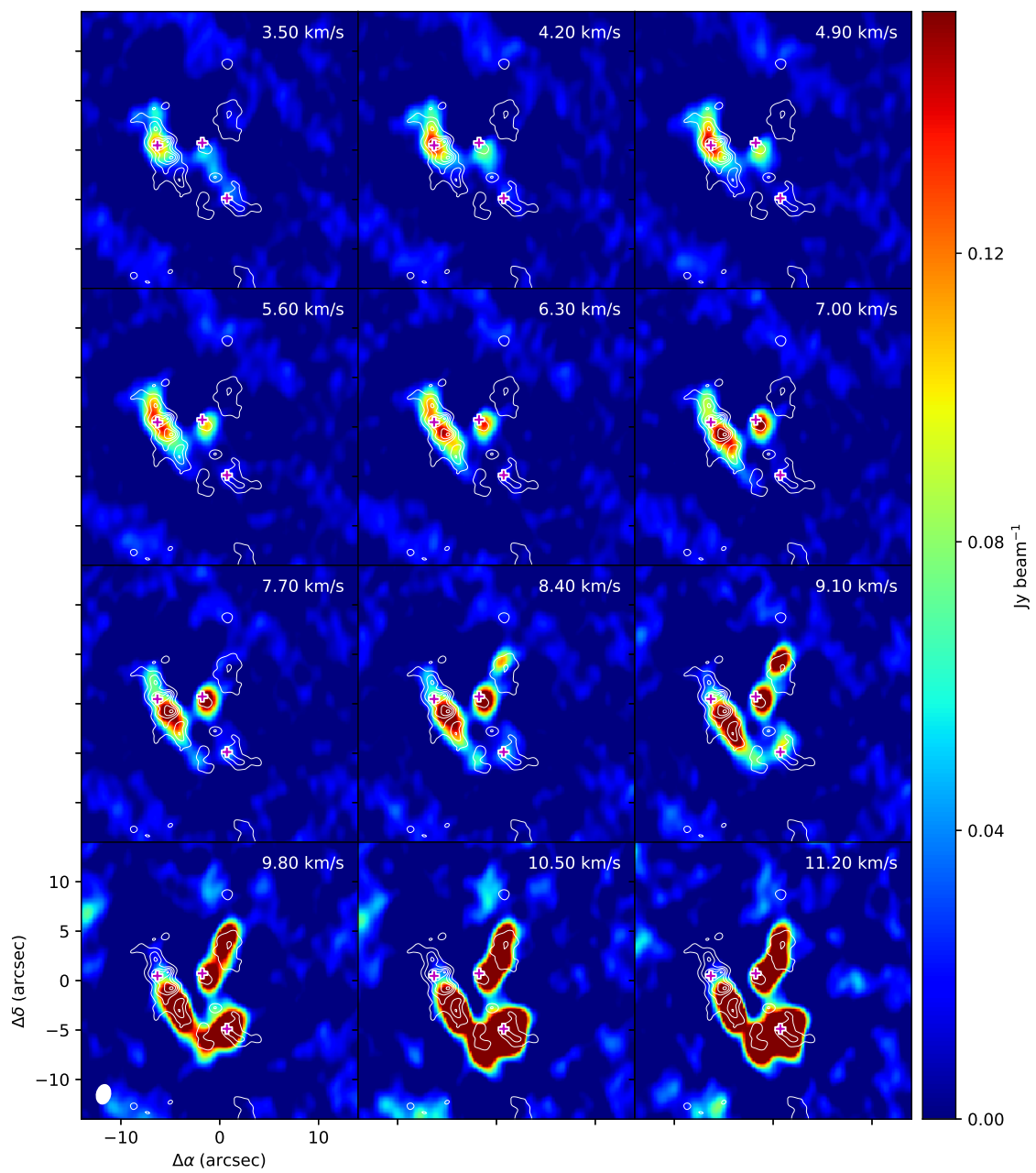


Figure A.11: 227.997GHz

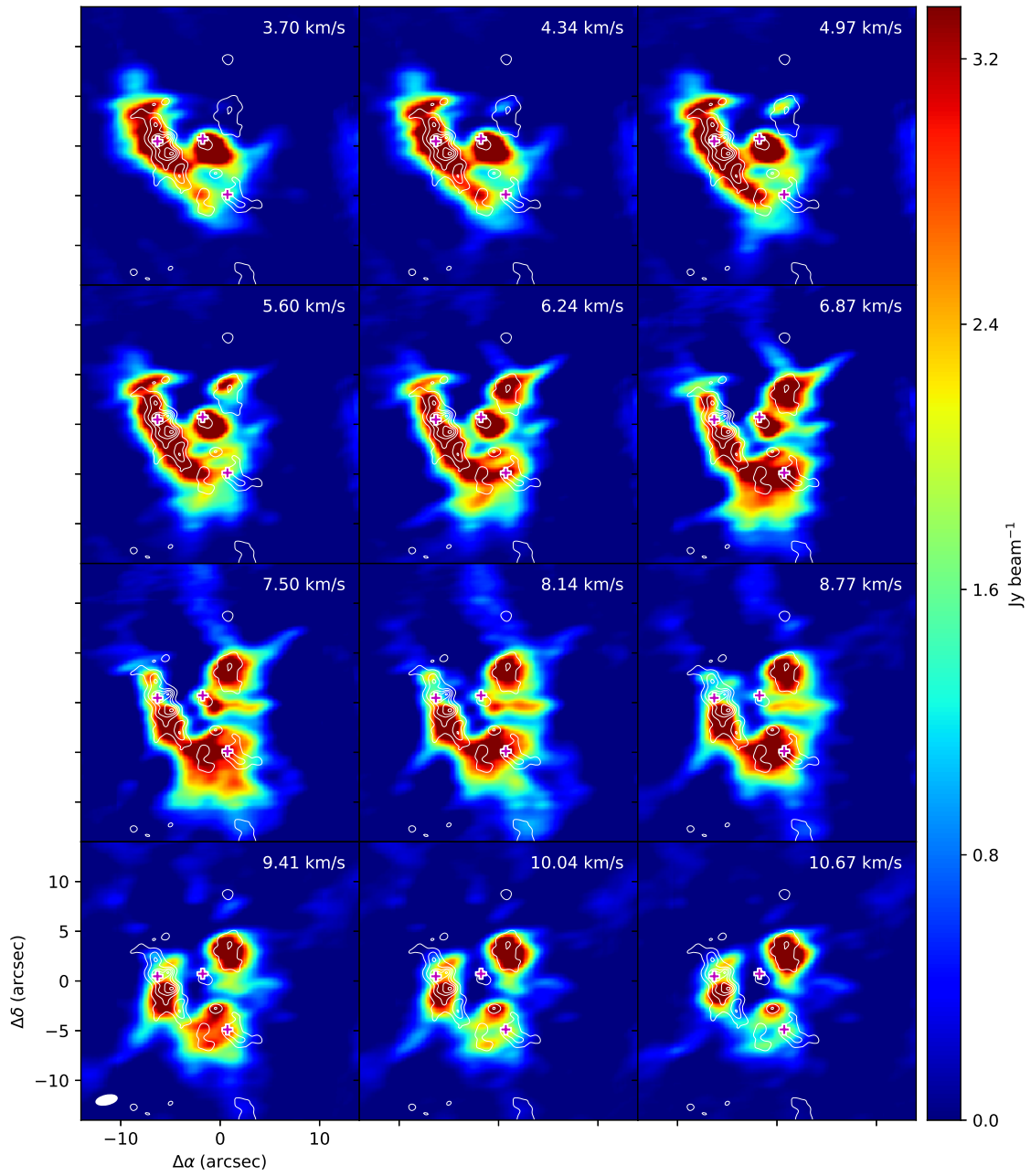


Figure A.12: 231.061GHz

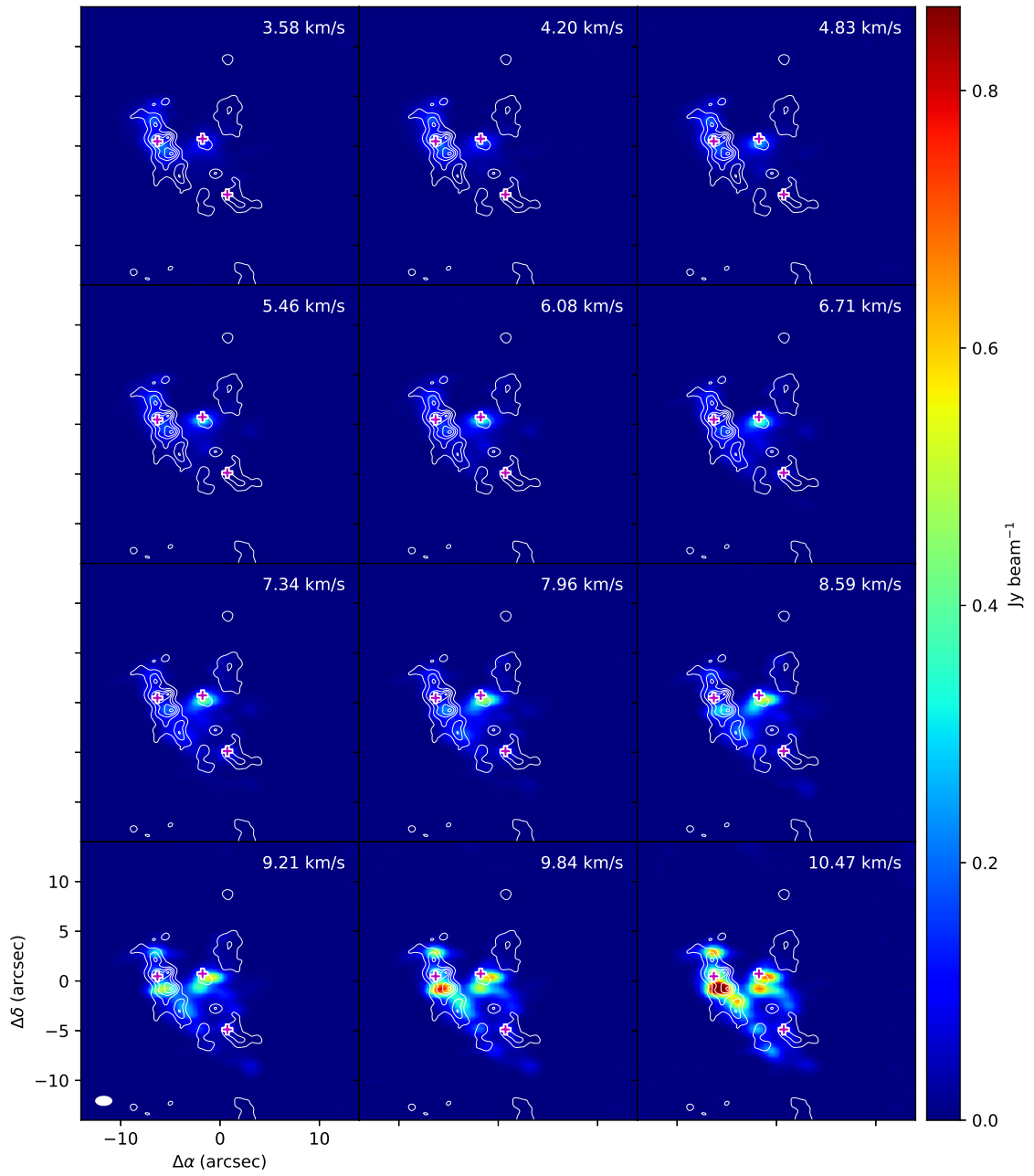


Figure A.13: 233.802GHz

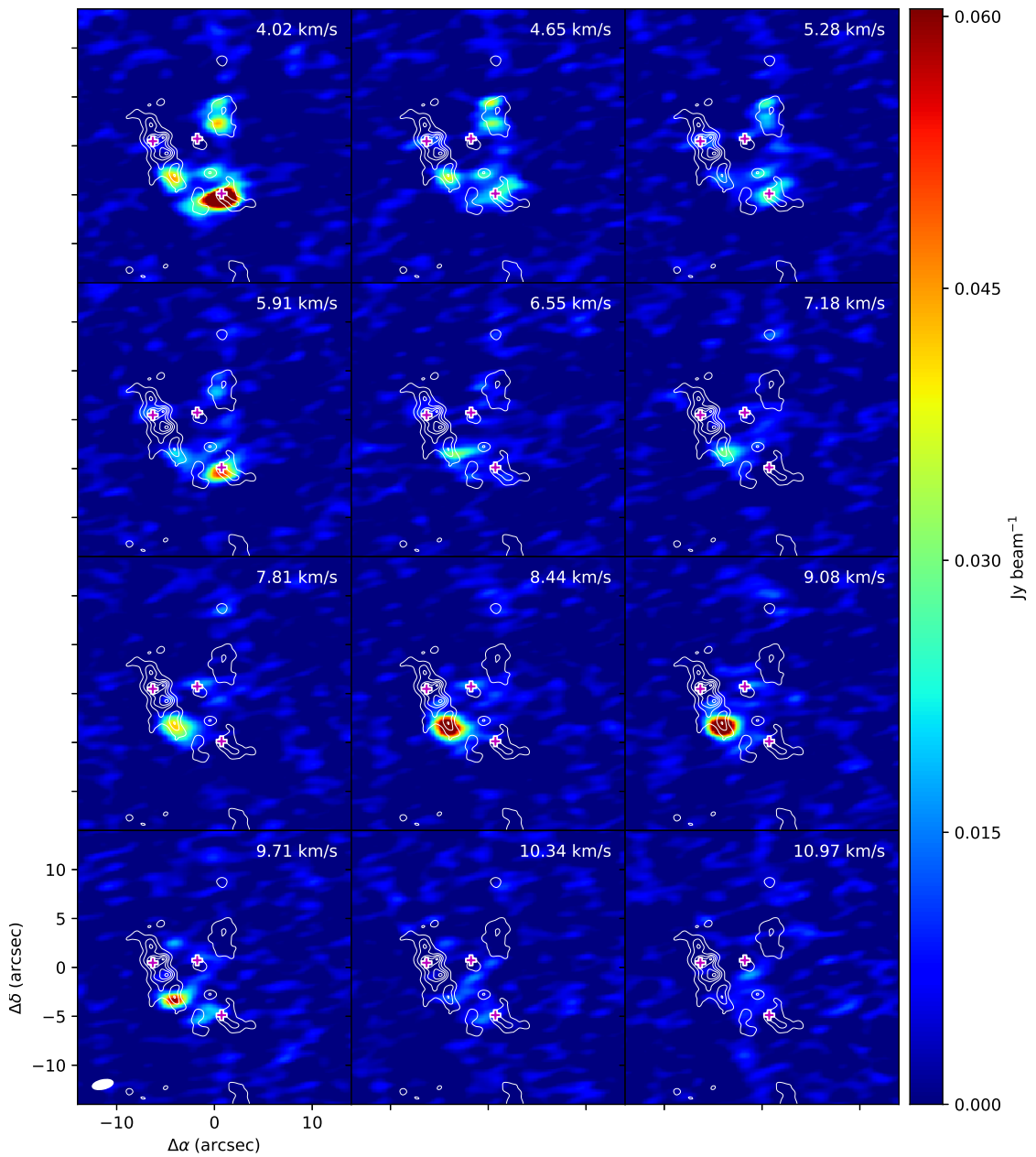


Figure A.14: 231.576GHz

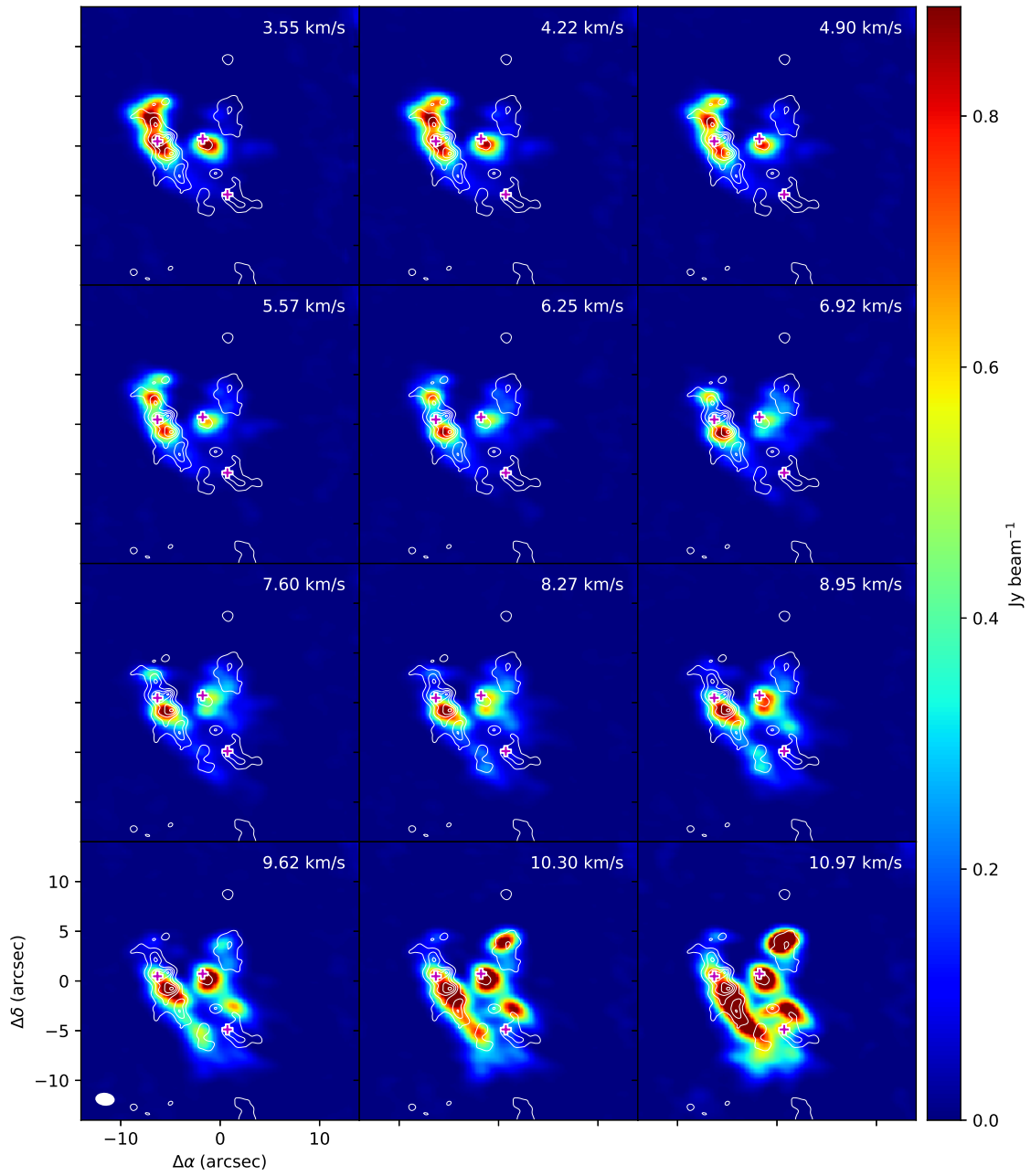


Figure A.15: 216.843GHz

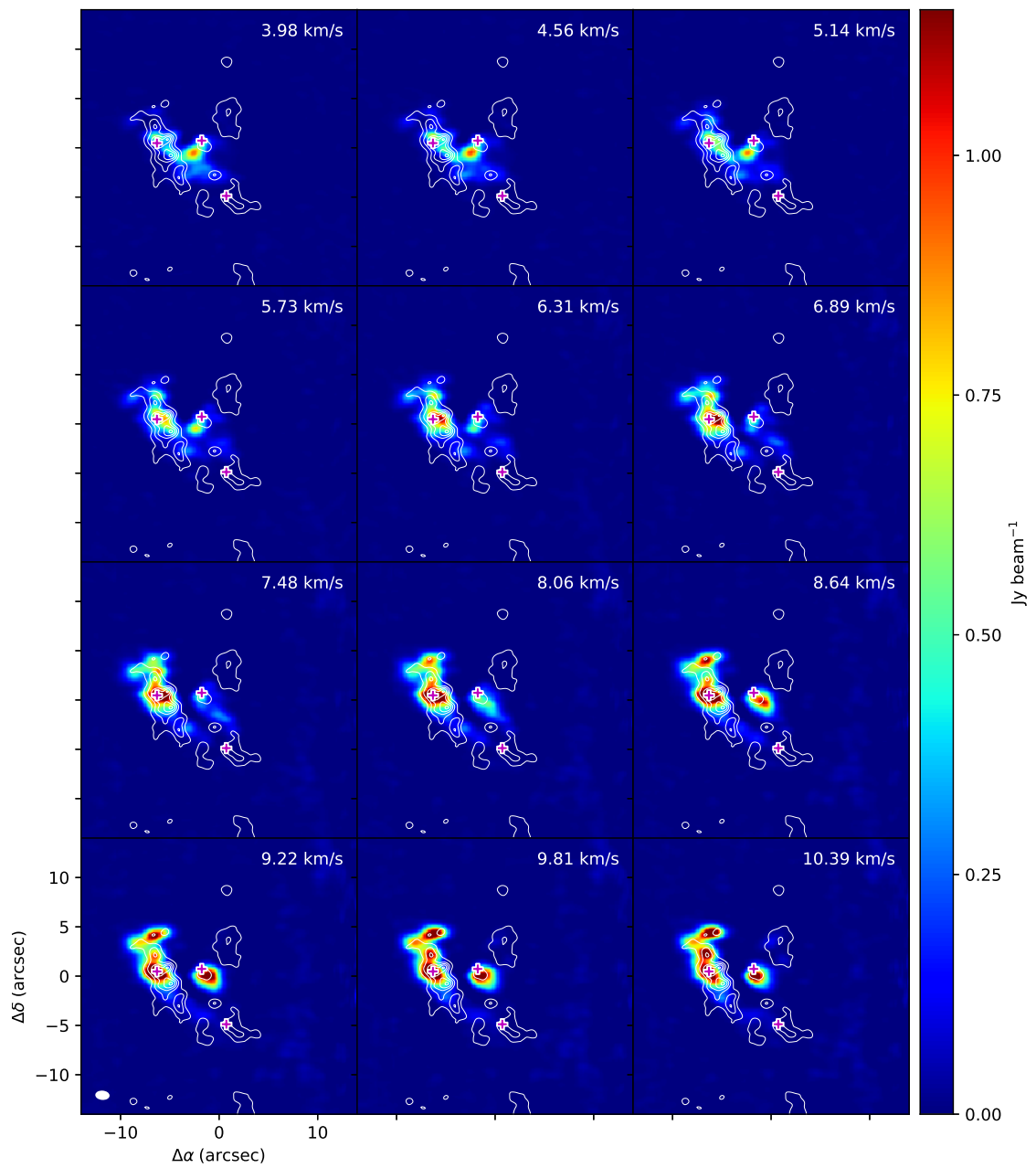


Figure A.16: 251.128GHz

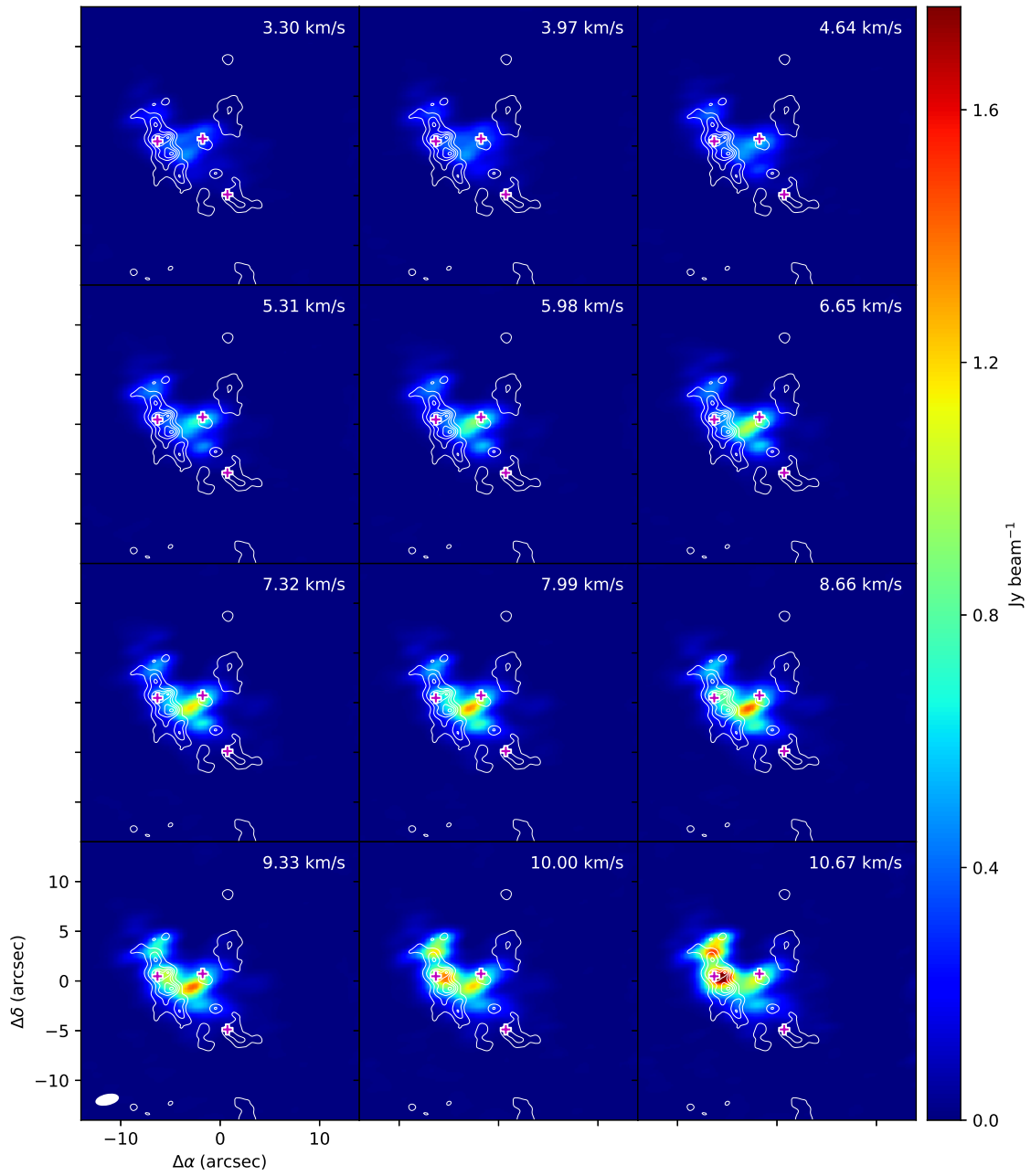


Figure A.17: 218.409GHz

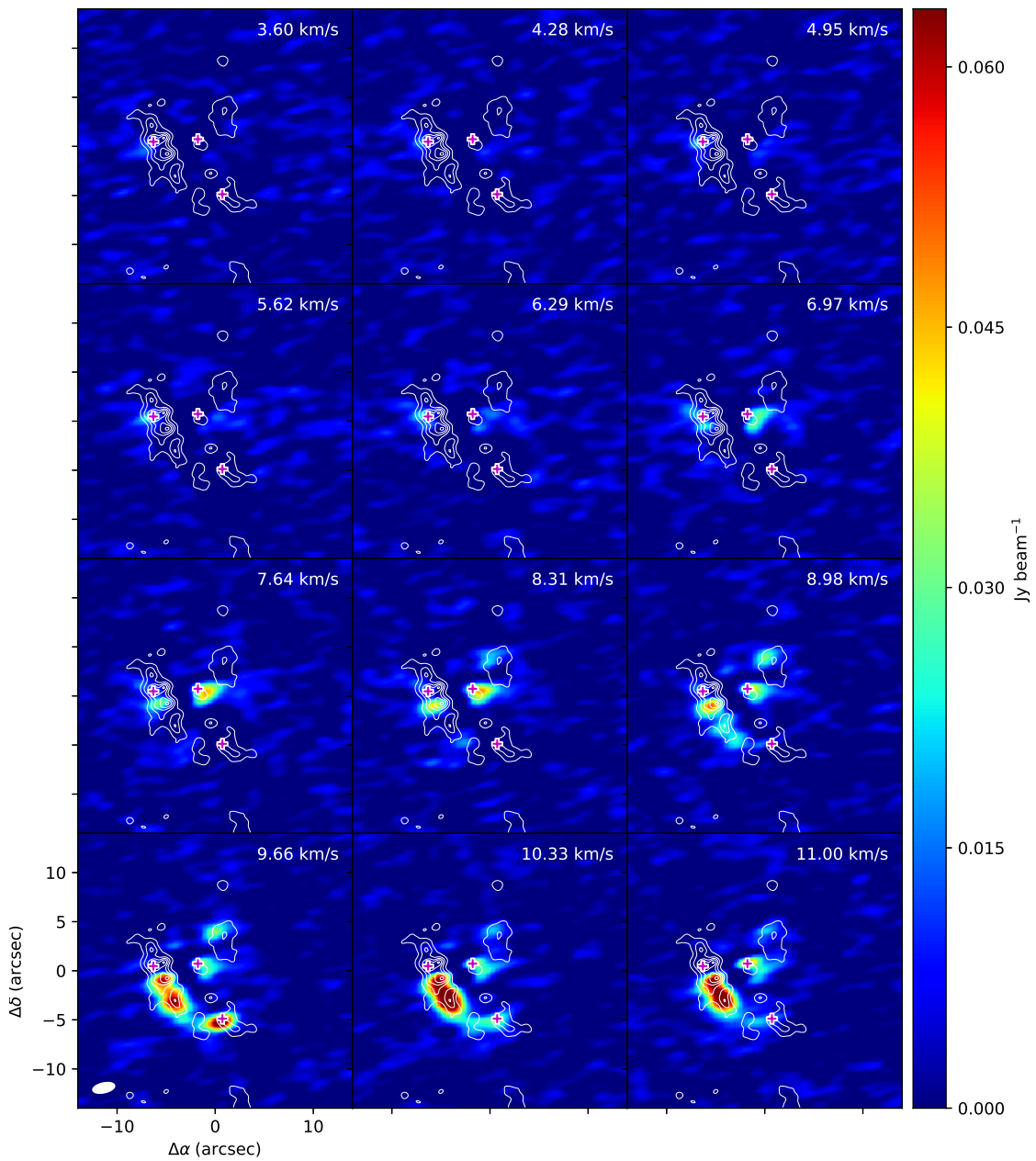


Figure A.18: 217.670GHz

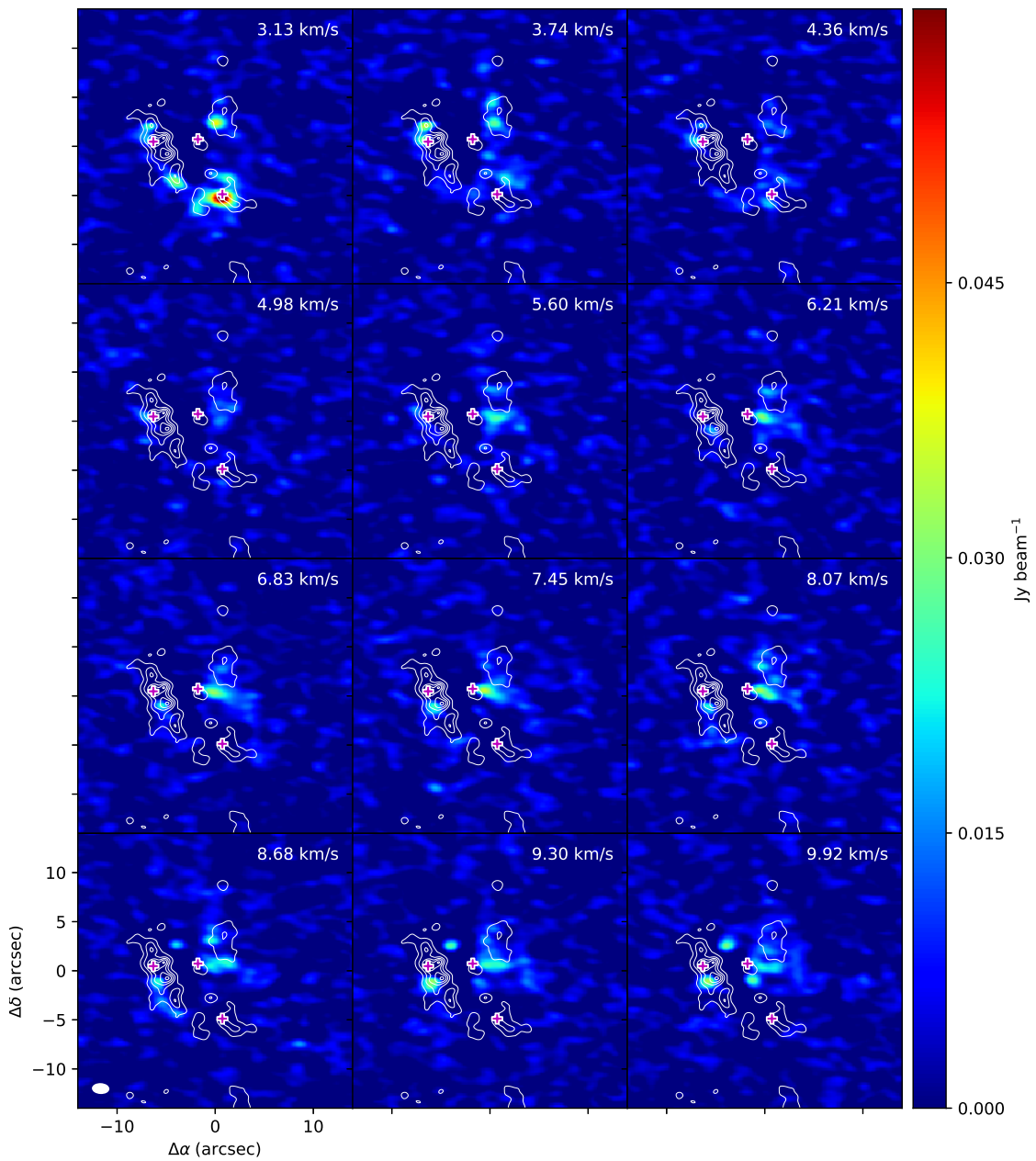


Figure A.19: 237.144GHz

Acknowledgments

References

- Hirota, T., Kim, M. K., Kurono, Y., & Honma, M. 2015, *The Astrophysical Journal*, 801, 82
- McMullin, J. P., Waters, B., Schiebel, D., Young, W., & Golap, K. 2007, in Astronomical Society of the Pacific Conference Series, Vol. 376, *Astronomical Data Analysis Software and Systems XVI*, ed. R. A. Shaw, F. Hill, & D. J. Bell, 127
- Pagani, L., Favre, C., Goldsmith, P. F., Bergin, E. A., Snell, R., & Melnick, G. 2017, *Astronomy & Astrophysics*, 604, A32
- Turner, B. E. 1991, *The Astrophysical Journal Supplement*, 76, 617